

# SharpNet: Enhancing MLPs to Represent Functions with Controlled Non-differentiability

Hanting Niu <sup>\*1 2</sup> Junkai Deng <sup>\*3</sup> Fei Hou <sup>1 2</sup> Wencheng Wang <sup>1 2</sup> Ying He <sup>3</sup>

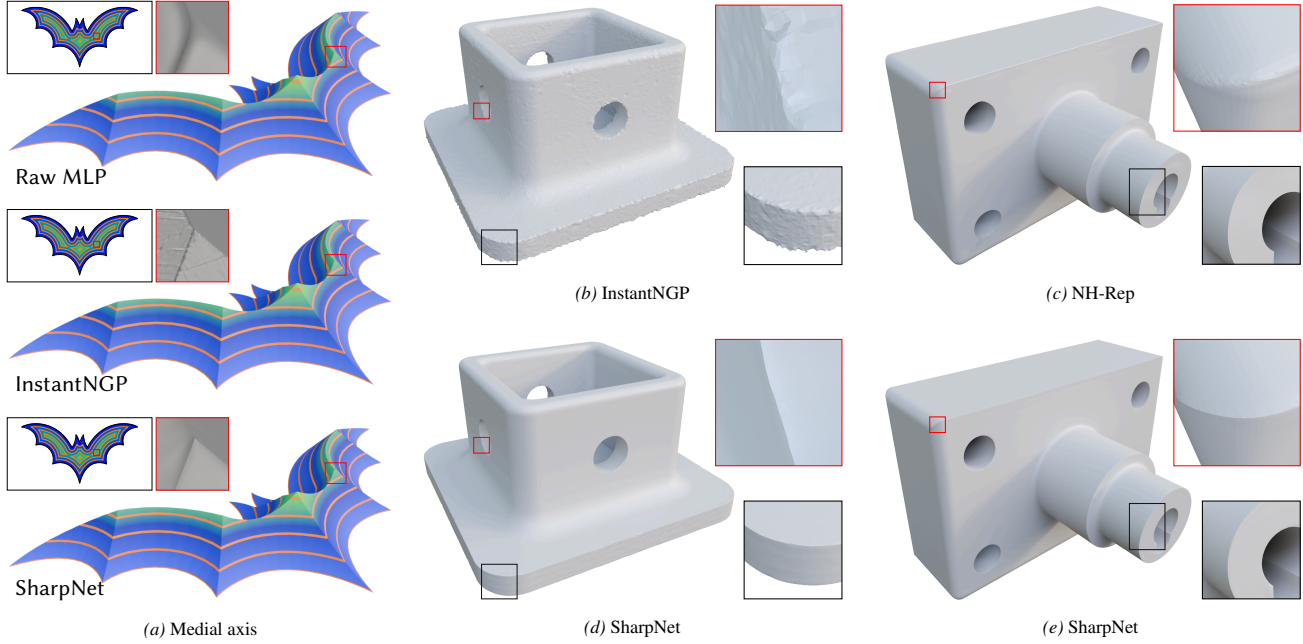


Figure 1. MLPs and sinusoidal-activation networks such as SIRENs (Sitzmann et al., 2020) are effective at representing smooth functions; SharpNet extends these architectures to model functions with sharp ( $C^0$ ) features at user-specified locations. (a) Distance field of a 2D closed curve, which is non-differentiable along the medial axis. We visualize the field using both a 2D colormap and a height-field rendering; the height-field view more clearly reveals the field’s non-smooth behavior of Instant NGP (Müller et al., 2022). (b,c) Reconstruction of a CAD model from a mesh input. NH-Rep (Guo et al., 2022) constructs the CAD model through patch subdivision and forms sharp edges via patch intersections, but it is unable to represent open (non-closed) sharp edges. (d,e) Reconstruction of a CAD model from points and normals input. InstantNGP (Müller et al., 2022) introduces notable artifacts, particularly around sharp edges. In contrast, without the requirements of patch subdivision or grid subdivision, SharpNet can generate strictly  $C^0$ -continuous sharp features, regardless whether they are closed or not.

## Abstract

Multi-layer perceptrons (MLPs) are a standard tool for learning and function approximation, but they inherently yield outputs that are globally smooth. As a result, they struggle to represent functions that are continuous yet deliberately non-

differentiable (i.e., with prescribed  $C^0$  sharp features) without relying on ad hoc post-processing. We present **SharpNet**, a modified MLP architecture capable of encoding functions with user-defined sharp features by enriching the network with an auxiliary *feature function*, which is defined as the solution to a Poisson equation with jump Neumann boundary conditions. It is evaluated via an efficient local integral that is fully differentiable with respect to the feature locations, enabling our method to jointly optimize both the feature locations and the MLP parameters to recover the target functions/models. The

<sup>\*</sup>Equal contribution <sup>1</sup>Institute of Software, Chinese Academy of Sciences, China <sup>2</sup>University of Chinese Academy of Sciences, China <sup>3</sup>College of Computing and Data Science, Nanyang Technological University, Singapore. Correspondence to: Fei Hou <houfei@ios.ac.cn>, Ying He <yhe@ntu.edu.sg>.

$C^0$ -continuity of SharpNet is precisely controllable, ensuring  $C^0$ -continuity at the feature locations and smoothness elsewhere. We validate SharpNet on 2D problems and 3D CAD model reconstruction, and compare it against several state-of-the-art baselines. In both types of tasks, SharpNet accurately recovers sharp edges and corners while maintaining smooth behavior away from those features, whereas existing methods tend to smooth out gradient discontinuities. Both qualitative and quantitative evaluations highlight the benefits of our approach.

## 1. Introduction

Multi-layer perceptrons (MLPs) are fundamental building blocks of modern deep learning and are particularly effective at approximating smooth functions. Their expressive power and differentiability have made them a standard choice in geometry and vision (Mescheder et al., 2019; Pang et al., 2023). In 3D shape modeling, MLPs support neural signed distance functions (SDFs) that continuously represent surfaces in space (Park et al., 2019; Ma et al., 2021; Wang et al., 2022; Li et al., 2023). In novel view synthesis, they serve as the core function approximators in neural radiance fields (NeRFs) (Mildenhall et al., 2020) and related methods for multi-view 3D reconstruction (Wang et al., 2021). In these settings, differentiability is central: it enables efficient gradient-based optimization and facilitates learning continuous, well-behaved fields.

However, many real-world targets are not globally smooth. In particular, several tasks require representing *sharp* geometric features, where the function is continuous but its derivative changes abruptly. A common example is CAD reconstruction from unoriented point clouds (Dong et al., 2024), where sharp edges and corners are as important as smooth surfaces to preserve geometric fidelity. From a functional point of view, such structures correspond to  $C^0$  behavior with discontinuities in the gradient, which conventional MLP parameterizations struggle to reproduce reliably.

This limitation is closely tied to activation regularity. MLPs with smooth activations (e.g., softplus, sigmoid, or tanh) are  $C^\infty$  and therefore cannot represent true non-differentiabilities. ReLU-based MLPs are only  $C^0$  and can, in principle, represent gradient discontinuities through their piecewise-linear structure. However, they do not provide clear control over *where* these non-differentiabilities occur, which is a problem when sharp features must align with known or learnable geometry.

We introduce **SharpNet**, an MLP variant designed to represent functions that are smooth almost everywhere while exhibiting non-differentiability at specific locations. Sharp-

Net augments the network input with a geometric prior: an auxiliary *feature function* that captures the desired set of sharp features. We define this feature function as the solution to a Poisson equation with jump Neumann boundary conditions, resulting in a field that is smooth away from the feature set and  $C^0$ -continuous with a normal derivative discontinuity along it. This construction draws on classical PDE theory and Green’s third identity, which reduces to a boundary integral with a closed-form formulation for numerical computation.

Our framework applies both when feature geometry is available and when it must be inferred. If sharp feature locations are known, the feature function is fixed during training. When the feature geometry is unknown, The feature locations and MLP parameters are trained in an end-to-end framework as our feature function is fully differentiable.

We validate SharpNet on both 2D and 3D problems. In 2D, we evaluate distance function learning and medial axis learning, where the latter corresponds precisely to the non-differentiable feature curves. In 3D, we test SharpNet on learning CAD models under three distinct setups, covering both fixed and learnable sharp features. In all cases, SharpNet attains superior accuracy in the vicinity of non-differentiable regions. By comparison, raw MLPs and Instant NGP (Müller et al., 2022) consistently fail to represent these sharp structures. NH-Rep (Guo et al., 2022) must partition the surface into multiple patches and derive sharp edges via their intersections, making it difficult to handle open (non-closed) sharp edges. As illustrated in Figure 1, SharpNet accurately reproduces the intended non-differentiable behavior, whereas the baseline architectures have significant difficulties.

## 2. Related Works

### 2.1. Improving Representation Capabilities of MLPs

The representational power of neural networks has been studied extensively, most notably through universal approximation theorems (Cybenko, 1989; Hornik, 1991). These results establish that MLPs can approximate broad classes of functions, but they say comparatively little about how well (or how efficiently) neural networks capture *non-smooth* structures such as kinks, corners, or discontinuities.

Several works have begun to address this gap. Imaizumi and Fukumizu (Imaizumi & Fukumizu, 2019) analyze approximation error and convergence rates for deep ReLU networks on function classes that include non-smooth targets. While their theory characterizes when good approximation is possible, it does not provide a mechanism for explicitly *placing* non-smoothness at prescribed geometric locations, which is critical in many geometry-processing settings. Ismailov (Ismailov, 2023) further shows that three-

layer neural networks can approximate both continuous and discontinuous functions, expanding the theoretical understanding of what shallow networks can represent.

A complementary line of work improves practical representation quality by augmenting MLPs with structured encodings. InstantNGP (Müller et al., 2022) and NGLOD (Takikawa et al., 2021) discretize the domain using a grid and learn feature values at grid vertices; features at arbitrary locations are obtained by (tri)linear interpolation. Such hybrid representations can greatly increase effective capacity and training speed, but their interpolants are still constrained by the underlying cell structure. In particular, because they rely on cellwise interpolation over a fixed grid, they do not provide a principled way to impose *exact*  $C^0$  features: functions that are continuous while showing controlled, geometry-aligned gradient discontinuities, as in our construction.

Most closely related to our goal are discontinuity-aware neural fields for 2D domains (Belhe et al., 2023; Liu et al., 2025a). To represent functions with discontinuities at specific locations (e.g., image edges), Belhe et al. (2023) uses a fixed triangulation and assigns separate feature values to each side of a triangle edge, creating discontinuities through barycentric interpolation. Liu et al. (2025a) generalizes this idea by making the discontinuity boundaries learnable, allowing more flexible modeling of structured discontinuities. These methods are well designed for function discontinuities, as commonly encountered in image domains where color values jump across boundaries. In contrast, our setting targets  $C^0$  functions with discontinuities in the gradient. When adapted to  $C^0$ -continuous targets, their barycentric, mesh-based interpolation ties non-smoothness to the entire triangulation. As a result, sharpness is not confined to the desired feature geometry but “leaks” onto other mesh boundaries, whereas our *meshless* formulation precisely localizes  $C^0$  features to the specified set.

A concurrent work is (Liu et al., 2025b), which introduces a  $C^0$ -continuous neural network for subspace physics. Because the unsigned distance function (UDF) is  $C^0$ -continuous on the zero level set, their method directly uses the UDF as the  $C^0$ -continuous feature function. However, the UDF defined on the medial axis of the zero level-set surface is also  $C^0$ -continuous. In contrast, we introduce a fully controllable  $C^0$ -continuous feature function that is strictly  $C^0$ -continuous on the feature surface and  $C^\infty$ -continuous everywhere else.

Liu et al. (2025c) proposes Kolmogorov–Arnold Networks (KANs), which replace fixed node-wise activations with learnable edge-wise activation functions. KANs have shown strong empirical performance on function approximation, often matching or surpassing larger MLPs with fewer parameters. That said, KANs are primarily evaluated on smooth

targets, and their behavior in modeling and *controlling* sharp ( $C^0$  but non- $C^1$ ) features remains largely unexplored.

## 2.2. Neural CAD Models

Most CAD reconstruction methods aim to recover *explicit* representations defined by analytic primitives and their relationships. Boundary representation (B-rep) models a solid via its bounding surfaces and their adjacency/topology (Liu et al., 2024b; Li et al., 2025; Shen et al., 2025; Usama et al., 2026), emphasizing accurate surface fitting and consistent patch connectivity. Constructive solid geometry (CSG), in contrast, seeks to infer a shape’s construction program as a sequence/tree of Boolean operations (Du et al., 2018; Dupont et al., 2025). Such procedural descriptions are flexible, editable, and closely aligned with manual CAD workflows.

Alongside these analytic approaches, a growing body of work learns *implicit* CAD representations using multi-layer perceptrons, typically in the form of signed distance fields (SDFs) or occupancy fields. Patch-based implicit methods such as NH-Rep (Guo et al., 2022) and Patch-Grid (Lin et al., 2025) compose multiple learned implicit functions (often one per surface patch) using CSG-style merging to recover sharp edges and corners. However, these approaches typically rely on a given patch decomposition and therefore do not directly address feature discovery from raw, unsegmented inputs.

Other methods incorporate CAD-specific priors using standard MLPs. NeurCADRecon (Dong et al., 2024) fits an SDF from unoriented point clouds with a developability prior (encouraging near-zero Gaussian curvature) to better match piecewise-developable CAD surfaces. NeuVAS (Wang et al., 2025) targets variational surface modeling under sparse geometric control and supports  $G^0$  sharp feature curves specified by input curve sketches. Despite these advances, controlling *where* non-differentiability occurs remains challenging for standard MLP parameterizations.

In contrast, we propose an implicit neural representation that is *explicitly* designed to model  $C^0$  sharp features at prescribed (or learned) locations while remaining smooth elsewhere. Table 1 summarizes representative CAD modeling and reconstruction approaches.

## 3. SharpNet

Let  $\Phi_\theta$  denote an MLP with parameters  $\theta$  that represents a function  $\Phi_\theta : \Omega \subset \mathbb{R}^{d+n} \rightarrow \mathbb{R}^m$ . Unless stated otherwise, we assume smooth activation functions, so  $\Phi_\theta$  is  $C^\infty$  with respect to its inputs. The spatial input dimension  $d$ , the auxiliary feature dimension  $n$ , and the output dimension  $m$  are arbitrary; in this paper, we focus on 2D and 3D settings with scalar-valued outputs, i.e.,  $d \in \{2, 3\}$  and  $m = 1$ .

| Type     | Method                               | Input              | Structure                                  | Output       | Sharpness |
|----------|--------------------------------------|--------------------|--|--------------|-----------|
| Explicit | Point2CAD (Liu et al., 2024b)        | Point cloud        | Segmentation + analytic fitting            | B-rep        | Yes       |
|          | Split-and-Fit (Liu et al., 2024a)    | Point cloud        | Voronoi                                    | B-rep        | Yes       |
|          | Mesh2Brep (Shen et al., 2025)        | Mesh               | Primitive fitting + constraints            | B-rep        | Yes       |
|          | FR-CSG (Chen et al., 2025)           | Mesh               | Primitive fitting + Optimization           | CSG tree     | Yes       |
|          | D <sup>2</sup> CSG (Yu et al., 2023) | 3D model           | Unsupervised learning                      | CSG tree     | Yes       |
|          | CAPRI-Net (Yu et al., 2022)          | Point cloud        | Self-supervised learning                   | CSG tree     | Yes       |
|          | CSGNet (Sharma et al., 2022)         | 2D/3D model        | RNN  | CSG program  | Yes       |
|          | (Wu et al., 2018)                    | Point cloud        | Primitive fitting + Optimization           | CSG tree     | Yes       |
|          | InverseCSG (Du et al., 2018)         | 3D model           | Program synthesis / search                 | CSG tree     | Yes       |
|          | TransCAD (Dupont et al., 2025)       | Point cloud        | Sequence model                             | CAD sequence | Yes       |
| Implicit | NURBGen (Usama et al., 2026)         | Text               | LLM-driven NURBS modeling                  | B-rep        | Yes       |
|          | SIREN (Sitzmann et al., 2020)        | Point cloud        | MLP (periodic activations)                 | SDF          | No        |
|          | NGLOD (Takikawa et al., 2021)        | SDF                | MLP + octree/grid features + interpolation | SDF          | Limited   |
|          | InstantNGP (Müller et al., 2022)     | SDF                | MLP + hash-grid encoding + interpolation   | SDF          | Limited   |
|          | NH-Rep (Guo et al., 2022)            | Subdivided Patches | MLP + neural halfspaces + Boolean tree     | SDF          | Yes       |
|          | Patch-Grid (Lin et al., 2025)        | Subdivided Patches | MLP + patch SDFs + CSG merge grid          | SDF          | Yes       |
|          | NeurCADRecon (Dong et al., 2024)     | Point cloud        | MLP + developability prior                 | SDF          | No        |
|          | NeuVAS (Wang et al., 2025)           | Curve sketches     | MLP + variational regularization           | SDF          | Yes*      |
|          | SharpNet (ours)                      | Point cloud        | MLP + feature function (PDE)               | SDF          | Yes       |

Table 1. High-level comparison of representative CAD reconstruction and modeling methods. SIREN, NGLOD, and InstantNGP are general-purpose neural field architectures applicable beyond CAD; here we list them specifically in the context of CAD shape representation and reconstruction. “Limited” indicates that sharpness is not explicitly localized to the true feature geometry (e.g., it may be grid-/cell-aligned or resolution-limited). \*NeuVAS models  $G^0$  sharp curves specified by input sketches.

For convenience, we consider the case where the auxiliary feature dimension is set to  $n = 1$ .

Let  $M \subset \Omega$  be a (possibly non-manifold) curve or surface on which we require the represented function to remain continuous but non-differentiable. To encode the locations of such sharp features, we introduce an auxiliary *feature function*  $f : \Omega \rightarrow \mathbb{R}$  that is non-differentiable exactly on  $M$  and smooth elsewhere. We incorporate  $f$  into the network by concatenating  $f(\mathbf{x})$  with the spatial coordinates  $\mathbf{x}$ . We denote the resulting  $f$ -augmented MLP by  $\Phi_\theta(\mathbf{x}, f(\mathbf{x}))$ , referred to as SharpNet.

### 3.1. Propagation of Non-differentiability under Composition

Our approach relies on the fact that non-differentiability in the input map  $\mathbf{x} \mapsto f(\mathbf{x})$  can be transferred to the composed field  $\mathbf{x} \mapsto \Phi_\theta(\mathbf{x}, f(\mathbf{x}))$ , provided that the network is locally sensitive to the feature channel. This idea is formalized below.

**Theorem 3.1.** *Assume  $M$  is codimension one in  $\Omega$ . Let  $f$  be differentiable on  $\Omega \setminus M$  and non-differentiable on  $M$ . Assume  $\Phi_\theta(\mathbf{x}, u)$  is differentiable with respect to  $(\mathbf{x}, u)$ , and that  $\partial \Phi_\theta / \partial u$  does not vanish on  $M$  (i.e., the network locally depends on the feature channel). Then the composed function  $\mathbf{x} \mapsto \Phi_\theta(\mathbf{x}, f(\mathbf{x}))$  is differentiable on  $\Omega \setminus M$  and non-differentiable on  $M$ .*

Although non-differentiability often propagates through function composition, it is not guaranteed in full generality. In particular, there are two common mechanisms by

which a composite function may remain differentiable: **(1) Feature insensitivity.** If the composed model does not depend on the feature channel (e.g., the weights associated with  $f$  vanish), then the output reduces to a function of  $\mathbf{x}$  alone, which is equivalent to replacing  $f$  with a constant zero function. In this case, the composite function is differentiable everywhere. **(2) Local flattening.** Even when the model depends on  $f$ , the non-differentiability of  $f$  can be canceled if the outer function has zero partial derivative with respect to  $f$  at the non-differentiable point of  $f$ . A simple example is  $f(t) = |t|$ , which is not differentiable at  $t = 0$ , but  $g(f(t)) = f(t)^2 = t^2$  is differentiable because  $g'(0) = 0$ .

In summary, provided that the network is sensitive to the feature channel when  $\mathbf{x} \in M$ , the non-differentiability along  $M$  is inherited by the composed field  $\Phi(\mathbf{x}, f(\mathbf{x}))$ . The condition,  $\partial \Phi / \partial f \neq 0$  on (or almost everywhere on)  $M$ , is almost always satisfied in practical applications, and thus SharpNet is generally effective at representing non-differentiable features.

### 3.2. Feature Function

#### 3.2.1. DEFINITION

To define the feature function  $f$ , which is twice differentiable everywhere except along the normal of a set  $M$  of codimension one in  $\Omega$ , i.e.,  $\mathbf{x} \in M$  is the first kind discontinuity of the normal directional derivative of  $f$ , we consider Poisson’s equation:

$$\nabla^2 f(\mathbf{x}) = h(\mathbf{x}), \quad \mathbf{x} \in \Omega \setminus M \quad (1)$$

subject to the following conditions on  $M$ :

- Jump Neumann boundary condition:

$$\frac{\partial f(\mathbf{x})}{\partial \mathbf{n}_{\mathbf{x}}^+} - \frac{\partial f(\mathbf{x})}{\partial \mathbf{n}_{\mathbf{x}}^-} = g(\mathbf{x}), \quad \mathbf{x} \in M \setminus \partial M \quad (2)$$

- Continuity condition:

$$\lim_{\mathbf{y} \rightarrow \mathbf{x}} f(\mathbf{y}) = f(\mathbf{x}), \quad \mathbf{x} \in M \quad (3)$$

Here,  $h(\mathbf{x})$  is continuous for all  $\mathbf{x} \in \Omega \setminus M$ .  $\partial M$  denotes the boundary of  $M$ . The vector  $\mathbf{n}_{\mathbf{x}}$  denotes the unit normal at a point  $\mathbf{x} \in M$ , and the one-sided normal derivative of  $f(\mathbf{x})$  in the direction of  $\mathbf{n}_{\mathbf{x}}$  is defined as:

$$\frac{\partial f(\mathbf{x})}{\partial \mathbf{n}_{\mathbf{x}}^{\pm}} = \lim_{\epsilon \rightarrow 0^{\pm}} \frac{f(\mathbf{x} + \epsilon \mathbf{n}_{\mathbf{x}}) - f(\mathbf{x})}{\epsilon}.$$

Since  $M$  is not necessarily a manifold, the normal vector  $\mathbf{n}_{\mathbf{x}}$  is defined only at manifold points  $\mathbf{x} \in M$ . In particular, at non-manifold points, such as Y-junctions in 2D or points on non-manifold edges in 3D, the normal vector is not well-defined. For the function  $g$ , we only require  $g(\mathbf{x}) \neq 0$  for  $\mathbf{x} \in M \setminus \partial M$ , which ensures discontinuities in the normal derivatives along the feature set.

We formalize the regularity of the feature function  $f$  defined by the above conditions in the following theorem:

**Theorem 3.2.** *Equations (1) to (3) provide the necessary and sufficient conditions for a function  $f(\mathbf{x})$  to be  $C^0$ -continuous along  $M$  and twice differentiable elsewhere in  $\Omega$ .*

### 3.2.2. CONSTRUCTION

The solution to Poisson's equation (1) can be expressed using a boundary integral formulation via the third Green's identity (Costabel, 1987):

$$f(\mathbf{x}) = \int_{\Omega} h(\mathbf{y}) G_{\mathbf{x}}(\mathbf{y}) dV_{\mathbf{y}} + \int_M g(\mathbf{y}) G_{\mathbf{x}}(\mathbf{y}) dS_{\mathbf{y}}, \quad (4)$$

where  $dV$  and  $dS$  are the volume and surface (area) elements, respectively. The function  $G_{\mathbf{x}}(\mathbf{y})$  is the Green's function of the Laplacian operator evaluated at the observation point  $\mathbf{x}$ . It takes the following forms:

- In 2D:

$$G_{\mathbf{x}}(\mathbf{y}) = \frac{1}{2\pi} \ln \|\mathbf{x} - \mathbf{y}\|,$$

- In 3D:

$$G_{\mathbf{x}}(\mathbf{y}) = -\frac{1}{4\pi \|\mathbf{x} - \mathbf{y}\|}.$$

To simplify the computation of the feature function  $f$ , we consider a special case where  $h(\mathbf{x}) = 0$  and  $g(\mathbf{x}) = 1$ . Under this setting, Equation (4) reduces to:

$$f(\mathbf{x}) = \int_M G(\mathbf{x}, \mathbf{y}) dS_{\mathbf{y}}. \quad (5)$$

In both 2D and 3D, the integrals of Green's function over line segments and triangular faces admit closed-form solutions. Therefore, when  $M$  is represented as a polyline (in 2D) or a triangular mesh (in 3D), the feature function  $f$  can be computed by summing the contributions of individual line segments or triangles.

### 3.2.3. ACCELERATION

Equation (5) integrates on the feature curves  $M$  (in 2D) or all feature surfaces  $M$  (in 3D), which is computationally expensive. We can subdivide  $M$  into a set of disjoint subregions  $M_i$  and  $\cup_i M_i = M$ ,

$$f(\mathbf{x}) = \int_M G(\mathbf{x}, \mathbf{y}) dS_{\mathbf{y}} = \sum_{M_i} \int_{M_i} G(\mathbf{x}, \mathbf{y}) dS_{\mathbf{y}}.$$

We can know that  $f_i(\mathbf{x}) = \int_{M_i} G(\mathbf{x}, \mathbf{y}) dS_{\mathbf{y}}$  is  $C^0$ -continuous for  $\mathbf{x} \in M_i$  and  $C^{\infty}$ -continuous for  $\mathbf{x} \in \Omega \setminus M_i$ . Let  $\phi_i(\mathbf{x})$  be a  $C^{\infty}$ -continuous function. We define

$$f_i(\mathbf{x}) = \phi_i(\mathbf{x}) \int_{M_i} G(\mathbf{x}, \mathbf{y}) dS_{\mathbf{y}}.$$

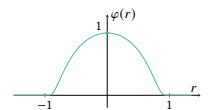
Then,  $f_i(\mathbf{x})$  is also  $C^0$ -continuous for  $\mathbf{x} \in M_i$  and  $C^{\infty}$ -continuous for  $\mathbf{x} \in \Omega \setminus M_i$ . We define the new feature

$$f(\mathbf{x}) = \sum_i f_i(\mathbf{x}) = \sum_i \phi_i(\mathbf{x}) \int_{M_i} G(\mathbf{x}, \mathbf{y}) dS_{\mathbf{y}}. \quad (6)$$

Apparently,  $f(\mathbf{x})$  is  $C^0$ -continuous for  $\mathbf{x} \in M$  and  $C^{\infty}$ -continuous for  $\mathbf{x} \in \Omega \setminus M$ . Equation (6) inspires us that we can reduce the global integration of Equation (5) to a local integration if the function  $\phi_i(\mathbf{x})$  satisfies the following conditions: (1)  $\phi_i(\mathbf{x})$  is  $C^{\infty}$ -continuous; (2)  $\phi_i(\mathbf{x})$  is compactly supported, i.e.,  $\phi_i(\mathbf{x})$  is nonzero only in a bounded set.

A mollifier is a smooth function with a compact support. A typical example of a mollifier is

$$\varphi(r) = \begin{cases} \frac{1}{I_n} e^{-\frac{1}{1-r^2}} & |r| < 1 \\ 0 & |r| \geq 1 \end{cases}$$



where  $I_n$  is a constant setting to  $1/e$  in experiments. A key property is that  $\varphi(r)$  is infinitely differentiable for  $r \in \mathbb{R}$ .

Let  $d(\mathbf{x}, M_i)$  denote the distance from a point  $\mathbf{x}$  to a local surface  $M_i$ , with the property that it increases as the point

$\mathbf{x}$  departs from  $M_i$ . Typically,  $M_i$  corresponds to a line segment in 2D and a triangular face in 3D. Let  $c(M_i)$  denote the center of  $M_i$ , defined as the average of its two endpoints in 2D or its three vertices in 3D. We define  $d(\mathbf{x}, M_i) = \|\mathbf{x} - c(M_i)\|^2$ , where the squared form ensures the smoothness of  $d(\mathbf{x}, M_i)$ . Let  $r = d(\mathbf{x}, M_i)$  and thus  $\phi_i(\mathbf{x}) = \varphi(d(\mathbf{x}, M_i))$ . Because both  $\varphi(r)$  and  $d(\mathbf{x})$  are smooth functions,  $\phi_i(\mathbf{x})$  is  $C^\infty$ -continuous and thus satisfies the two aforementioned conditions.

### 3.3. Network Design

Define  $D\partial_{\mathbf{n}}\Phi = \frac{\partial}{\partial \mathbf{n}_x^+}\Phi(\mathbf{x}, \mathbf{f}(\mathbf{x})) - \frac{\partial}{\partial \mathbf{n}_x^-}\Phi(\mathbf{x}, \mathbf{f}(\mathbf{x}))$  as the jump of the directional derivatives across  $M$ . A noteworthy property is that  $D\partial_{\mathbf{n}}\Phi$  does not depend on the direction in which  $M$  is crossed; i.e., it is the same whether one uses  $\mathbf{n}$  or  $-\mathbf{n}$ . Indeed,

$$\begin{aligned} \frac{\partial}{\partial(-\mathbf{n})_x^+}\Phi(\mathbf{x}, \mathbf{f}(\mathbf{x})) &= -\frac{\partial}{\partial \mathbf{n}_x^-}\Phi(\mathbf{x}, \mathbf{f}(\mathbf{x})), \\ \frac{\partial}{\partial(-\mathbf{n})_x^-}\Phi(\mathbf{x}, \mathbf{f}(\mathbf{x})) &= -\frac{\partial}{\partial \mathbf{n}_x^+}\Phi(\mathbf{x}, \mathbf{f}(\mathbf{x})), \end{aligned}$$

and therefore

$$\begin{aligned} D\partial_{-\mathbf{n}}\Phi &= \frac{\partial}{\partial(-\mathbf{n})_x^+}\Phi - \frac{\partial}{\partial(-\mathbf{n})_x^-}\Phi \\ &= -\frac{\partial}{\partial \mathbf{n}_x^-}\Phi + \frac{\partial}{\partial \mathbf{n}_x^+}\Phi = D\partial_{\mathbf{n}}\Phi. \end{aligned} \quad (7)$$

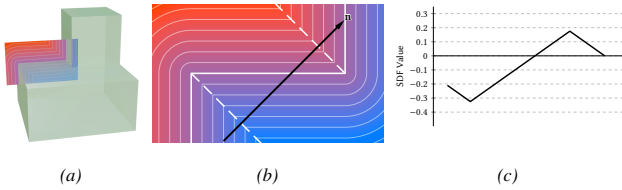


Figure 2. The cuboid-like shape in (a) features several sharp edges with right dihedral angles. We consider a cross-section that passes through both convex and concave edges. In (b), the SDF on this cross-section is visualized, and we select a line segment perpendicular to the medial axis; the SDF values along this segment are plotted in (c). From the SDF profile along this line, we see that medial-axis points corresponding to locally convex surface regions induce a concave SDF curve, which manifests as a positive jump in the directional derivative. In contrast, medial-axis points within locally concave surface regions give rise to a convex SDF curve, leading to a negative jump in the directional derivative.

Using the example illustrated in Figure 2, we see that the sign of  $D\partial\Phi$  is governed by whether  $\Phi$  is locally convex or concave. When  $\Phi$  is locally concave,  $D\partial\Phi$  is positive, whereas when  $\Phi$  is locally convex,  $D\partial\Phi$  becomes negative.

Even when the local shape remains either concave or convex—so the sign of  $D\partial\Phi$  does not change—the magnitude of  $D\partial\Phi$  can still exhibit abrupt jumps at junctions, as illustrated in Figure 3(a). On the other hand, at the corners of a

3D model, the sharp concave and convex edges can meet, resulting in the intersection of the convex and concave SDFs, causing a sign change in  $D\partial\Phi$ , as depicted in Figure 3(b). At these locations,  $D\partial\Phi$  is discontinuous.

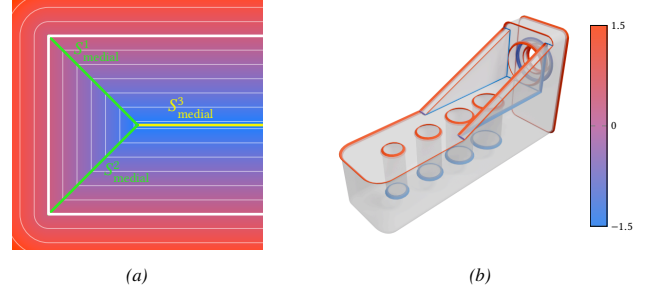


Figure 3. For a watertight surface  $S$  in either 2D or 3D, the SDF may exhibit directional derivative discontinuities across the medial axis or medial surface  $S_{\text{medial}}$  at junctions. If we define the sign convention of the SDF such that it is positive outside  $S$  and negative inside, then convex portions of  $S$  correspond to positive directional derivative jumps on the interior medial axis, while concave portions of  $S$  correspond to negative directional derivative jumps on the exterior medial axis. (a) Medial axes carrying different directional derivative jump values may converge at a same point. The branches  $S_1^{\text{medial}}$  and  $S_2^{\text{medial}}$  have the same jump magnitude of  $\sqrt{2}$ , whereas the jump increases to 2 suddenly along  $S_3^{\text{medial}}$ . (b) In 3D, positive and negative directional derivative jumps can meet at junction points whose local neighborhoods resemble saddle surfaces. For a CAD model, by coloring the medial surface near sharp edges according to the directional derivative jump values, multiple saddle-like junctions can be observed.

To enhance SharpNet’s ability to represent discontinuous  $D\partial\Phi$ , we divide  $M$  into disjoint subsets  $\{M^{(i)}\}_{i=1}^n$  such that  $M = \cup_{i=1}^n M^{(i)}$ . Note that  $M^{(i)}$  is not necessarily connected. For every subset  $M^{(i)}$ , we compute a corresponding feature function  $\mathbf{f}^{(i)}(\mathbf{x})$ . We then redefine SharpNet as  $\Phi(\mathbf{x}, \mathbf{f}^{(1)}(\mathbf{x}), \dots, \mathbf{f}^{(n)}(\mathbf{x}))$ , which enables the network to model discontinuous differences of the directional derivative across the boundaries of  $M^{(i)}$ . Let  $\Phi_{\mathbf{f}^{(i)}}$  denote the partial derivative of  $\Phi(\mathbf{x}, \mathbf{f}^{(1)}(\mathbf{x}), \dots, \mathbf{f}^{(n)}(\mathbf{x}))$  with respect to  $\mathbf{f}^{(i)}(\mathbf{x})$ . From the chain rule, we can deduce that  $D\partial_{\mathbf{n}}\Phi = \Phi_{\mathbf{f}^{(1)}} D\partial_{\mathbf{n}}\mathbf{f}^{(1)}(\mathbf{x}) + \dots + \Phi_{\mathbf{f}^{(n)}} D\partial_{\mathbf{n}}\mathbf{f}^{(n)}(\mathbf{x})$ . When  $\mathbf{x} \in M^{(i)}$ , only the  $i$ -th term contributes because  $D\partial_{\mathbf{n}}\mathbf{f}^{(i)}(\mathbf{x}) = 0$  for  $\mathbf{x} \notin M^{(i)}$ . Consequently,  $D\partial_{\mathbf{n}}\Phi = \Phi_{\mathbf{f}^{(i)}} D\partial_{\mathbf{n}}\mathbf{f}^{(i)}(\mathbf{x})$ ,  $\mathbf{x} \in M^{(i)}$ . Therefore,  $D\partial_{\mathbf{n}}\Phi$  may be discontinuous along the boundaries of  $M^{(i)}$ , but can remain continuous if  $\Phi_{\mathbf{f}^{(i)}}$  is appropriately constrained.

For subsequent 2D applications, our feature set is composed of line segments connecting vertices, which can be interpreted topologically as an undirected graph. We assume that jumps of directional derivative differences on the feature set  $M$  can only occur at junctions, i.e., vertices with degree greater than or equal to three. Consequently, the partitioning of  $M$  is reformulated as a coloring problem: assign colors to the edges of  $M$  such that at each junction all incident edges

have distinct colors. The objective is to use as few colors as possible (in practice, only a relatively small number is required to avoid excessively high feature dimensionality).

A similar partitioning strategy is also employed for the 3D applications. For learning signed distance fields of CAD models, we generate strip-like structures from the sharp edges of the model. These strips serve as approximations of the local medial surface near the mesh boundary, forming the feature surface  $M$  such that the corresponding feature function exhibits directional derivative jumps in the vicinity of sharp edges. By applying the 2D partitioning procedure to the undirected graph composed of all sharp edges, we obtain a coloring of the sharp edges. Each segment of the strip-like structure in  $M$  corresponds to a sharp edge, thereby yielding a partition of  $M$  based on the edge coloring.

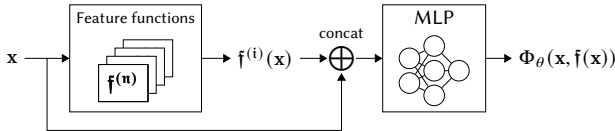


Figure 4. Architecture of SharpNet. The input coordinates are mapped by feature functions  $f^{(1)}, \dots, f^{(n)}$ , which are then concatenated with the original input coordinates and sent into an MLP that produces the final value.

**Remark** In this work, we adopt Poisson’s equation with jump Neumann boundary conditions to construct the feature function. While other types of functions may also be  $C^0$ -continuous at user-specified locations, they are not always suitable for our purpose. A commonly considered alternative is UDF (Liu et al., 2025b), where the user-specified set  $M$  is the zero level set of the UDF. In theory, UDF is  $C^0$ -continuous and non-differentiable at  $M$ . However, it also exhibits non-differentiability at other locations in the domain, specifically along the medial axis of  $M$ . (Liu et al., 2025b) alleviates the issue by converting the UDF  $d(\mathbf{p})$  using a smooth clamping function,

$$\|d(\mathbf{p})\|_{SC} = \begin{cases} \|d(\mathbf{p})\|_2 - \frac{1}{2s} \|d(\mathbf{p})\|_2^2, & \text{if } d(\mathbf{p}) < s, \\ \frac{1}{2}s, & \text{if } d(\mathbf{p}) \geq s. \end{cases}$$

Even though  $\|d(\mathbf{p})\|_{SC}$  eliminates the medial axis at  $d(\mathbf{p}) \geq s$ , the medial axis remains at  $d(\mathbf{p}) < s$ . Hence, the redundant  $C^0$ -continuity issue still exists.

In practice, the medial axis problem becomes significantly more severe. To evaluate the UDF, the feature surface  $M$  must first be discretized into a triangular mesh, and the UDF at a point  $\mathbf{p}$  is approximated by its distance to the nearest triangle face. This procedure generates a large number of medial axes, because every angular bisector plane formed by the convex angle between any pair of adjacent triangle faces constitutes a medial axis.

These extra discontinuities break the requirement that the feature function be differentiable on  $\Omega \setminus M$ , so the UDF does not fulfill Equation (1). Consequently, it is not a suitable candidate for defining our feature function. In addition, the smooth clamping function  $\|d(\mathbf{p})\|_{SC}$  is only  $C^1$ -continuous at  $d(\mathbf{p}) = s$ . In (Liu et al., 2025b), the feature surface  $M$  is not learnable, likely because computing the closest triangle face is not a differentiable operation. In contrast, our feature function  $f(\mathbf{x})$  is  $C^0$ -continuous on  $M$  and  $C^\infty$ -continuous elsewhere. Moreover,  $f(\mathbf{x})$  is differentiable with respect to  $M$ , which makes our feature surface  $M$  learnable.

## 4. Planar Applications

To assess SharpNet in 2D applications, we designed two experiments that target distinct aspects of performance. The first focuses on fitting accuracy, evaluating how well SharpNet fits geodesic distance fields when the feature curves are known. The second examines the learnability of feature curves, testing the model’s ability to learn medial axes when feature curves are unknown.

**Implementation and Baselines.** We configure SharpNet  $\Phi(\mathbf{x}, f(\mathbf{x}))$  with a standard MLP with Softplus activation, and compare against three corresponding baselines: a standard MLP without SharpNet module, SharpNet with ReLU activation and InstantNGP (Müller et al., 2022). In our implementations, the MLP consists of four hidden layers with 256 neurons each. The Softplus activation corresponds to the Softplus with  $\beta = 100$ . For InstantNGP used with Geodesic distance experiments, we use the default configuration except that we set the the number of levels as 8 instead of the default value of 16. We also remap the input coordinates to  $[0.0, 0.9]^2$  when encoding with InstantNGP. In all experiments except InstantNGP, we follow (Mildenhall et al., 2020) and use positional encoding to encode the input coordinates. In Geodesic experiments 4 frequencies are used for positional encoding; in Medial experiments 8 are used.

**Loss functions.** We optimize the parameters  $\theta$  of the neural network  $\Phi(\mathbf{x}, f(\mathbf{x}); \theta)$  by minimizing the following loss function,

$$\mathcal{L} = \mathcal{L}_F + \alpha \cdot \mathcal{L}_{\mathcal{R}}, \quad (8)$$

where  $\alpha$  (setting to 0.5 in our experiments) controls the relative weight of the regularization term. The term  $\mathcal{L}_F$  measures the mean absolute error between the network prediction and the ground-truth field values  $F(\mathbf{x}_i)$  across all  $k$  sampled points  $\{\mathbf{x}_i\}_{i=1}^k$ :

$$\mathcal{L}_F(\theta) = \frac{1}{k} \sum_{i=1}^k |F(\mathbf{x}_i) - \Phi(\mathbf{x}_i, f(\mathbf{x}_i); \theta)|$$

The regularization term  $\mathcal{L}_R$  is designed to keep uniform segments of polylines  $M$  and to prevent folding of  $M$ . Let  $\{\mathbf{a}_i\}_{i=1}^m$  denote the set of degree-2 vertices of  $M$ , and let  $\mathbf{a}_i^l$  and  $\mathbf{a}_i^r$  be the two neighboring vertices of each  $\mathbf{a}_i$ . We define

$$\mathbf{v}_i := \frac{\mathbf{a}_i^l + \mathbf{a}_i^r}{2} - \mathbf{a}_i, \quad \mathbf{u}_i := \frac{\mathbf{a}_i^r - \mathbf{a}_i^l}{\|\mathbf{a}_i^r - \mathbf{a}_i^l\|},$$

where  $\mathbf{v}_i$  is the differential coordinate (Sorkine, 2006) of the curve  $\mathbf{a}_i^l \mathbf{a}_i \mathbf{a}_i^r$ . The length of  $\mathbf{v}_i$  approximates the curvature at  $\mathbf{a}_i$ , and the direction of  $\mathbf{v}_i$  approximates the normal of  $\mathbf{a}_i$ .  $\mathbf{u}_i$  is the unit vector that points from  $\mathbf{a}_i^l$  to  $\mathbf{a}_i^r$ . The loss of regularization  $\mathcal{L}_R$  is defined by

$$\mathcal{L}_R(M) = \frac{\lambda}{m} \cdot \sum_{i=1}^m \|\mathbf{v}_i\| + \frac{1-\lambda}{m} \cdot \sum_{i=1}^m |\mathbf{v}_i \cdot \mathbf{u}_i|.$$

The first term encourages both uniform spacing of vertices along the curve and overall straightness. The second term preserves an even vertex distribution but permits flexible bending. We choose  $\lambda = 0.3$  to balance these two effects, keeping the  $M_i$  uniform while still allowing for slight curvature.

#### 4.1. Geodesic Distances Fitting

As illustrated in Figure 5, we consider a simple 2D setup where the source point is located at  $(0, 0)$ , and a disk of radius 0.5 centered at  $(1, 0)$  is removed from the domain. In this configuration, the resulting geodesic distance field is smooth throughout the domain except along a non-differentiable set  $M$ , which corresponds to the ray  $y = 0$  for  $x \geq 1.5$ . This setup provides a controlled test case, where the feature location  $M$  is assumed to be known. We use it to assess SharpNet’s ability to accurately represent geodesic distance fields with sharp transitions.

We evaluate both the baseline approaches and SharpNet variants using neural networks composed of 4 uniformly-sized layers of equal width of 256. Given the target function  $F$ , we train SharpNet following Equation (8) without including the regularization term  $\mathcal{L}_R(M)$ . A substantial amount of training data is sampled, with  $k = 1024^2$ . In InstantNGP, we map the coordinates into  $[0, 0.9]^2$  for hash indexing.

We report our results in Figure 5.  $\varepsilon$  below every figure denotes the error. In the top row, we evaluate the value accuracy of the learned geodesic distance field. We visualize the predicted distances within a narrow rectangular region ( $1.665 \leq x \leq 1.865, -0.025 \leq y \leq 0.025$ ). Since all methods behave similarly away from the sharp feature region  $M$ , we focus the evaluation on a tighter band ( $1.55 \leq x \leq 1.95, -0.005 \leq y \leq 0.005$ ) to highlight the ability to preserve non-differentiable structures and additionally report the absolute mean error of predict values in this

band. To aid visual comparison, iso-distance contours of the predicted field (orange solid lines) and the ground truth (white dashed lines) are overlaid. For the value accuracy comparisons, in Figure 5(b), the baseline method is overly smoothed at sharp corner. In (c), InstantNGP is jagged and exhibits unwanted sharpness. In (d), ReLU is better but it also contains unwanted sharpness. In (e), when Softplus activation is used, the result is truly smooth everywhere unless at specific locations. The effects of unwanted sharpness are more pronounced in the bottom row, where we present the learned geodesic field as a height mesh and render the surface of the mesh.

We additionally report the mean absolute error of the gradient of the predicted field and plot the error maps. For the gradient accuracy comparisons, in (g), the baseline method is smooth everywhere including the ridge. This results in a very dark red line at the center of the plotted gradient error map. In (h), InstantNGP produces unwanted  $C^0$  features that are aligned with hash encoding grids. This corresponds to grid-like artifacts and creases on the surface. The error of the gradient is very large such that the plotted gradient error map is almost red everywhere. In (i), for SharpNet with ReLU activation, the sharpness of the ReLU function at zero causes the surface to contain various creases that are clearly visible in the rendered mesh as well as in the plotted error map. Finally, in (j), for SharpNet with Softplus activation, the surface is smooth everywhere except the ridge, leading to the overall best fitting quality. We render all images in high resolution to support close-up examination.

The experimental results show that SharpNet consistently outperforms the baseline methods in terms of accuracy, demonstrating its capability to accurately represent non-differentiable sharp features.

#### 4.2. Learning Medial Axes

The medial axis of a closed shape  $S$  is closely related to geodesic distances because  $S$  defines the source set from which distances are computed. The medial axis consists of points in the domain that have more than one closest point on  $S$ .

Along the medial axis, the distance field is  $C^0$ -continuous and non-differentiable; therefore, the medial axis serves as the feature set  $M$  of the distance field. Given  $F$ , we jointly learn the shape of the feature curves  $M$  and  $\Phi$  using Equation (8), including the optional regularization term  $\mathcal{L}_R$ . Figure 6 illustrates the evaluation of our method on a 2D rectangle example, where we report the medial-axis error. In this experiment, we first partition the ground truth medial axis into 94 segments and perturb the location of the vertices to simulate initialization error. We train the neural network and the medial axis jointly for 300,000 iterations. During the first 10,000 iterations, we freeze the medial axis,

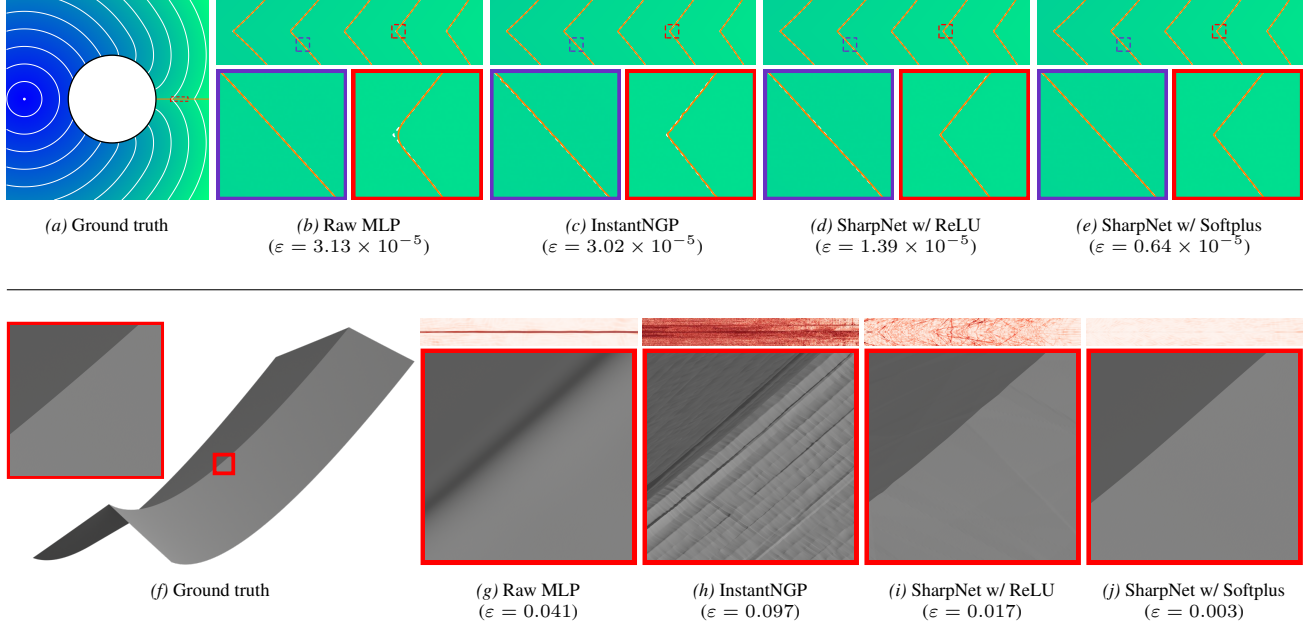


Figure 5. Evaluation of accuracy for training with known feature locations on a 2D geodesic distance field. Top: 2D visualization of the geodesic distance field with iso-distance curves; Bottom: Visualization of the geodesic distance field using height function, which can better reveal errors in the distances.

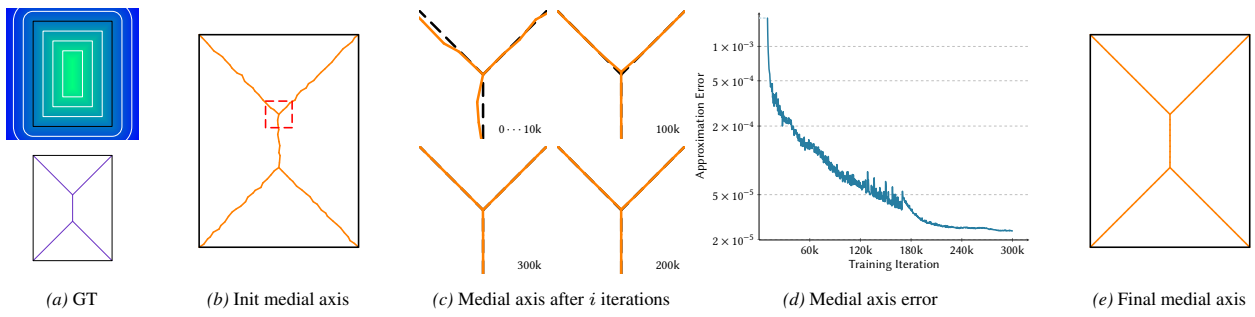


Figure 6. Evaluation of accuracy for training with inaccurate feature locations on the geodesic distance field of a rectangle. (a) Ground truth geodesic distance field, which is non-differentiable along the medial axis  $M$ , consisting of 5 segments as shown beneath it. (b) Initial feature estimate, composed of 94 segments, obtained by subdividing the ground-truth medial axis and perturbing the joint positions to simulate initialization error. (c) Close-up views of a Y-junction region, comparing initial feature and the progressively refined feature sets after 100k, 200k, and 300k training iterations (displayed clockwise). (d) Accuracy of the estimated feature set over the course of training. The medial axis in first 10k iterations is frozen and is marked with dashed line and faint color.

training the neural network alone to allow the network to focus on fitting the distance field without perturbing the coarse medial structure. After the initial frozen period, the medial axis is unfrozen, and all vertices with degree greater than one are optimized. We set the mollifier radius to 0.08 which is approximately four times the length of each medial axis segment.

### 4.3. Discussion of Alternatives

Our feature function  $f(x)$  ensures  $C^0$ -continuity for  $x \in M$  and  $C^\infty$ -continuity elsewhere. This makes an important distinction from closely relevant works including InstantNGP (Müller et al., 2022) and discontinuity-aware neural networks (DANN) (Belhe et al., 2023; Liu et al., 2025a). InstantNGP (Müller et al., 2022), while not specifically designed to reconstruct sharpness, follows a similar approach that encodes voxel-corner features in a hash table and performs linear interpolation within each voxel, providing significantly greater fitting capacity than a standard MLP. However, this linear interpolation enforces  $C^0$ -continuity across all voxel boundaries. As a result, unwanted  $C^0$ -continuity may appear at boundaries, while desired  $C^0$ -discontinuities inside a voxel cannot be represented. DANN, originally introduced by (Belhe et al., 2023) and later extended by (Liu et al., 2025a) to incorporate learnable curve features, can be interpreted as a two-dimensional, non-uniform, single-resolution variant of InstantNGP. DANN is not designed for sharp features either but rather designed for discontinuities. However, it shares the same idea as ours by augmenting the neural network with additional features. In this regard, it is possible to extend their idea for reconstructing sharpness by assigning the same feature to both sides of a discontinuous edge. However, since it can be construed as an extended version of InstantNGP, it shares the same problem that it may introduce unwanted sharpness at positions where it is required to be smooth.

In addition to the Geodesic experiments in Section 4.1 and Figure 5, we introduce yet another experiment to better illustrate our argument. We test the mesh-based method of DANN (Belhe et al., 2023), Liu et al. (2025a) and use them to fit a two-dimensional field that is continuous everywhere but non-differentiable at their feature locations. We render the field as a 3D height mesh and shade the mesh by normals as colors for better clarity. We train our SharpNet with Softplus activation, with ReLU activation, InstantNGP with Softplus activation, DANN with Softplus activation, and Liu et al. (2025a) with their default neural network to fit the field and their results are shown in Figure 7.

For DANN (Belhe et al., 2023) and Liu et al. (2025a), the trained field is non-differentiable at places where the features located, but is also non-differentiable elsewhere coinciding with the location of their mesh structure. For Instant-

NGP, the rendered mesh contains axis-aligned, horizontal and vertical artifacts which are very likely to be the boundaries of their multi-resolution grids. For SharpNet with ReLU activation function, the rendered mesh contains various creases that are caused by the non-differentiability of the ReLU activation function. Only our method, SharpNet with Softplus activation, learns a field that is smooth everywhere excepted at specified feature locations, hence achieving best fidelity.

## 5. CAD Applications

We illustrate the practicality of SharpNet using three representative CAD reconstruction tasks. The first examines the direct conversion of explicit CAD meshes into an implicit representation. This scenario emphasizes SharpNet’s capability to accurately encode sharp features when their locations are given. The second addresses a more challenging setting, where CAD models are reconstructed from point clouds augmented with oriented normal constraints. The third and most challenging setting reconstructs CAD models using only point cloud data. In the latter two scenarios, we simultaneously infer both the underlying CAD geometry and its sharp features, demonstrating SharpNet’s strength in sharp feature learning. Depending on the specific input type, we respectively adopt NH-Rep (Guo et al., 2022), InstantNGP (Müller et al., 2022), and NeurCADRecon (Dong et al., 2024) as baselines.

**Dataset** We conduct our evaluation on the same collection of 100 models used in (Erler et al., 2020), which are drawn from the ABC dataset (Koch et al., 2019). The testing models comprise intricate CAD geometries that exhibit a wide range of challenging features, including high-genus surfaces, thin structures, both open and closed sharp edges and curves, as well as other complex and irregular structural characteristics that thoroughly test the robustness of our method.

**Metrics** We use four metrics to evaluate the quality and accuracy of the learned CAD models: Chamfer Distance (CD), Hausdorff Distance (HD), Normal Error (NE), and F-1 Score (FC). Let  $\mathcal{P}_1, \mathcal{P}_2$  be two point sets obtained by sampling from the respective model surfaces, and let  $\|\mathcal{P}_i\|$  denote the cardinality of  $\mathcal{P}_i$ . For any point  $\mathbf{p} \in \mathbb{R}^3$ , we define

$$\text{NN}_{\mathcal{P}_i}(\mathbf{p}) := \arg \min_{\mathbf{q} \in \mathcal{P}_i} \|\mathbf{p} - \mathbf{q}\| \quad (i = 1, 2).$$

For any sample point  $\mathbf{p} \in \mathcal{P}_i$ , we denote its associated normal by  $\vec{n}_p$ . Let  $r$  be the distance threshold used to determine whether two points are considered a match. We define the metrics above as:

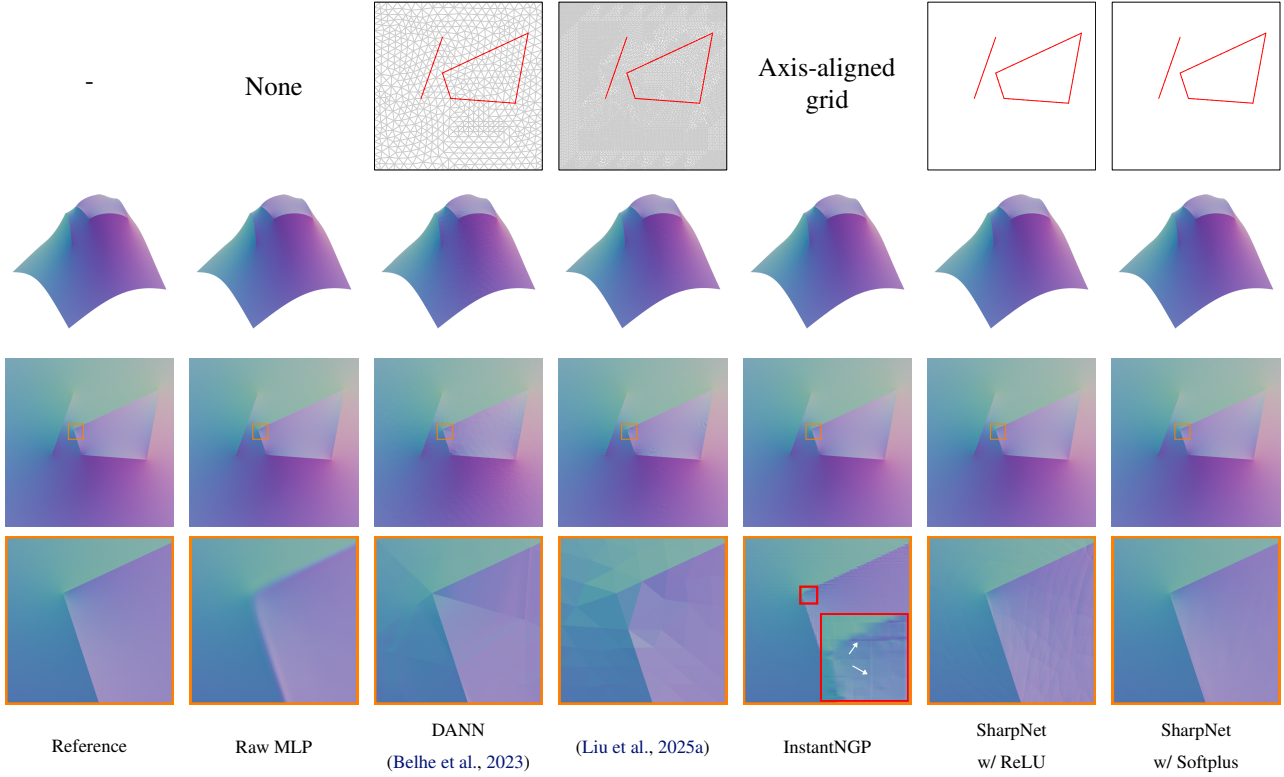


Figure 7. Comparisons against different representations of sharpness strategies. The first row shows the meshing and feature locations. The second to fourth rows display the learned 2.5D models along with locally zoomed-in views.

$$CD = \frac{\sum_{\mathbf{p} \in \mathcal{P}_1} \|\mathbf{p} - \text{NN}_{\mathcal{P}_2}(\mathbf{p})\|}{2\|\mathcal{P}_1\|} + \frac{\sum_{\mathbf{p} \in \mathcal{P}_2} \|\mathbf{p} - \text{NN}_{\mathcal{P}_1}(\mathbf{p})\|}{2\|\mathcal{P}_2\|},$$

$$HD = \max \left( \max_{\mathbf{p} \in \mathcal{P}_1} \|\mathbf{p} - \text{NN}_{\mathcal{P}_2}(\mathbf{p})\|, \max_{\mathbf{p} \in \mathcal{P}_2} \|\mathbf{p} - \text{NN}_{\mathcal{P}_1}(\mathbf{p})\| \right)$$

$$NE = \frac{\sum_{\mathbf{p} \in \mathcal{P}_1} \arccos |\vec{n}_{\mathbf{p}} \cdot \vec{n}_{\text{NN}_{\mathcal{P}_2}(\mathbf{p})}|}{2\|\mathcal{P}_1\|} + \frac{\sum_{\mathbf{p} \in \mathcal{P}_2} \arccos |\vec{n}_{\mathbf{p}} \cdot \vec{n}_{\text{NN}_{\mathcal{P}_1}(\mathbf{p})}|}{2\|\mathcal{P}_2\|},$$

$$FC = \frac{2R_1 R_2}{R_1 + R_2}, \text{ where } R_1 \text{ and } R_2 \text{ denote:}$$

$$R_1 = \frac{\|\{\mathbf{p} \in \mathcal{P}_1 | \|\mathbf{p} - \text{NN}_{\mathcal{P}_2}(\mathbf{p})\| < r\}\|}{\|\mathcal{P}_1\|},$$

$$R_2 = \frac{\|\{\mathbf{p} \in \mathcal{P}_2 | \|\mathbf{p} - \text{NN}_{\mathcal{P}_1}(\mathbf{p})\| < r\}\|}{\|\mathcal{P}_2\|}.$$

**Training details** For each model, we uniformly sample 50,000 surface points and rescale them to fit within the bounding box  $[-1, 1]^3$  centered at  $(0, 0, 0)$ . For every sampled point, the distance to its  $k$ -nearest neighbors in the point cloud ( $k = 50$ ) is used as the standard deviation of a Gaussian distribution from which additional neighbor samples are drawn. SIREN, InstantNGP, and SharpNet all use a 4-layer

256-width MLP and sine as activation function. In each epoch, we randomly select 20,000 points from the 50,000 surface samples and draw an additional 20,000 near-surface points using Gaussian perturbations around them. We also uniformly sample 10,000 points in the extended domain  $[-1.1, 1.1]^3$  as ambient points. The networks are trained for 15,000 epochs using the Adam optimizer (Kingma & Ba, 2015), with the specific loss function determined by each experiment. Finally, the mesh is extracted using Dual Contouring (Ju et al., 2002), which preserves sharp features.

### 5.1. Implicit Conversion of CAD Mesh Models

Implicit representation of CAD mesh models has several benefits over explicit representations, such as Boolean operations. SharpNet is able to utilize an MLP to learn and reconstruct CAD models with distinct sharp features. In contrast, other approaches (Guo et al., 2022; Lin et al., 2025) have to decompose the model into smaller sub-patches, applying multiple MLPs to represent them. Ultimately, they perform Boolean operations to merge these sub-patches for the reconstruction of sharp features.

We compare our method with NH-Rep (Guo et al., 2022), which partitions CAD meshes into sub-patches based on pre-defined input feature curves. Given the mesh as input,

we detect sharp feature curves based on the dihedral angles between neighboring faces. For SharpNet, we further define the feature surface  $M$  based on the collection of angular bisector planes along these sharp curves. Detailed information on the extraction of sharp curves and the subsequent generation of the sharp feature surface  $M$  can be found in Appendix A.

In this experiment, the features  $M$  remain invariant throughout the training process. We train SharpNet using common SDF learning losses.

$$\mathcal{L}(\theta) = \alpha_{\text{sur}} \cdot \mathcal{L}_{\text{sur}} + \alpha_{\text{ext}} \cdot \mathcal{L}_{\text{ext}} + \alpha_{\text{ekl}} \cdot \mathcal{L}_{\text{ekl}} + \alpha_{\text{nor}} \cdot \mathcal{L}_{\text{nor}}, \quad (9)$$

where  $\mathcal{L}_{\text{sur}}$ ,  $\mathcal{L}_{\text{ext}}$ ,  $\mathcal{L}_{\text{ekl}}$  and  $\mathcal{L}_{\text{nor}}$  are

$$\begin{aligned} \mathcal{L}_{\text{sur}}(\theta) &= \frac{1}{r} \sum_{i=1}^r |\Phi_{\theta}(\mathbf{x}_i, \mathbf{f}(\mathbf{x}_i))| \\ \mathcal{L}_{\text{ext}}(\theta) &= \frac{1}{s} \sum_{i=1}^s \exp(-\alpha |\Phi_{\theta}(\mathbf{x}_i, \mathbf{f}(\mathbf{x}_i))|) \\ \mathcal{L}_{\text{nor}}(\theta) &= \frac{1}{r} \sum_{i=1}^r \|\nabla \Phi_{\theta}(\mathbf{x}_i, \mathbf{f}(\mathbf{x}_i)) - \mathbf{n}_i\| \\ \mathcal{L}_{\text{ekl}}(\theta) &= \frac{1}{t} \sum_{i=1}^t |1 - \|\nabla \Phi_{\theta}(\mathbf{x}_i, \mathbf{f}(\mathbf{x}_i))\||. \end{aligned}$$

Because NH-Rep requires oriented normals as constraints, we also incorporate normals. Here,  $\mathbf{n}_i$  denotes the oriented normal associated with point  $\mathbf{x}_i$ .

At each training epoch, the surface loss  $\mathcal{L}_{\text{sur}}$  and the surface-normal loss  $\mathcal{L}_{\text{nor}}$  are evaluated on surface sampling points. The exterior loss  $\mathcal{L}_{\text{ext}}$ , which enforces the network output to stay away from zero far from the surface, is applied to ambient points. For the Eikonal loss  $\mathcal{L}_{\text{ekl}}$ , we use both surface samples and near-surface samples as inputs. The corresponding weight parameters are set to  $\alpha_{\text{sur}} = 7000$ ,  $\alpha_{\text{ext}} = 600$  and  $\alpha_{\text{ekl}} = 50$ .

**Non-closed sharp feature curves** NH-Rep (Guo et al., 2022) relies heavily on the assumption that feature curves are closed, enabling the model to be decomposed into patches and sharp features to be reconstructed via patch intersections. In practice, however, sharp feature curves are not always closed, as shown in Figure 8. When a patch includes such open sharp curves, it is left unsubdivided, which leads to the loss of the associated sharp features. More critically, as shown in Figure 9, open curves can generate a patch whose boundary includes a mix of concave and convex segments. In this situation, the min/max evaluation is no longer well-defined, and the construction of the CSG tree breaks down. Consequently, NH-Rep successfully processes only 65 out of 100 models (with some of the failures arising from other causes).

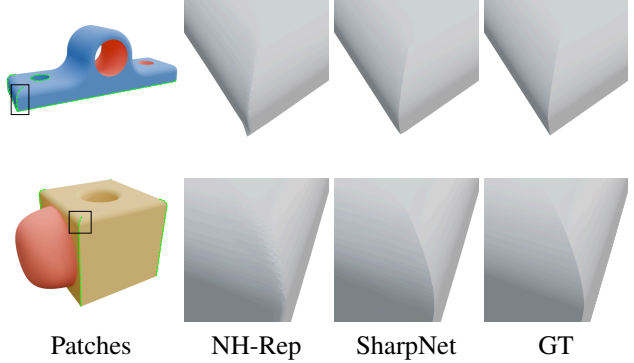


Figure 8. NH-Rep is unable to reconstruct open sharp feature curves due to its patch subdivision strategy. Dashed green curves are the sharp curves. The reconstruction results of NH-Rep, SharpNet, and the ground truth for the region indicated illustrate that the sharp curves of NH-Rep are smoothed.

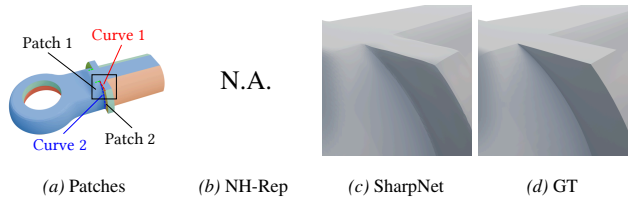


Figure 9. CSG tree construction of NH-Rep may fail in the presence of open sharp feature curves. (a) Due to open feature curves, under subdivision leads to some open feature curves to disappear in NH-Rep, as indicated in green dashed line. The boundary between Patch 1 and Patch 2 consists of both a convex sharp curve (Curve 1, blue dashed line) and a concave sharp curve (Curve 2, red dashed line), which makes the CSG min/max operation ambiguous. (b) As a result, NH-Rep does not produce valid outputs. (c)(d) show the reconstruction results of SharpNet and the ground truth for the boxed regions.

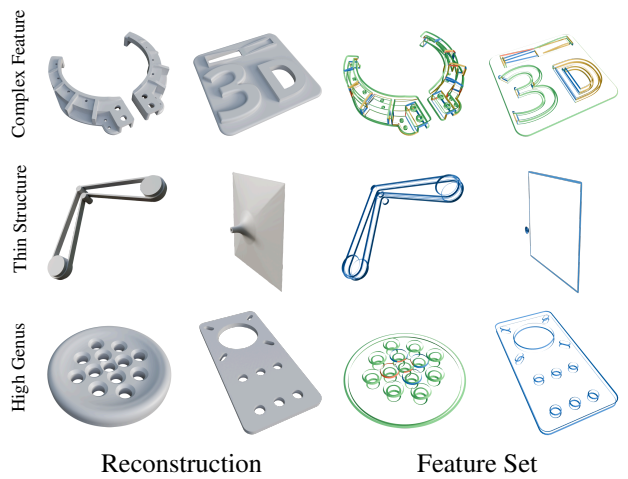


Figure 10. SharpNet performance in several challenging cases. The left column shows the reconstruction results, and the right column shows the corresponding sharp feature sets, where each color indicates one dimension of the feature function as defined in Section 3.3, following the feature-splitting scheme.

**Complex structures** Without the need for decomposition or meshing, SharpNet provides substantial flexibility in modeling gradient discontinuities, allowing it to represent a broad spectrum of intricate geometric forms. As shown in Figure 10, it supports feature curves of arbitrary shapes and connectivity, e.g., complex feature sets, thin-structures, and high-genus geometric shapes. In Figure 11, we compare the CD distributions and observe that the CDs of NH-Rep on high-genus models are noticeably large.

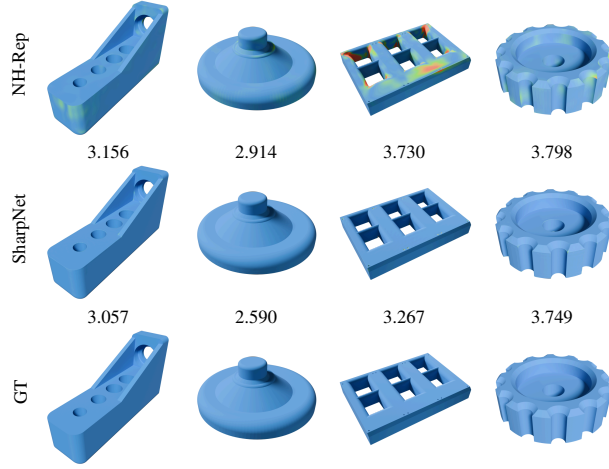


Figure 11. Illustration of CD errors visualized by a color map. The CD value for each model is shown below its reconstruction. The CD of NH-Rep is noticeably larger on one of the models due to the presence of open feature curves, exhibiting the same issue shown in Figure 8.

The quantitative results for all 65 models are summarized in Table 2. SharpNet surpasses NH-Rep across all four evaluation metrics. In addition, both NH-Rep and Patch-Grid handle sharp features as fixed entities, preventing them from being updated during training. By contrast, the sharp features in our SharpNet are learnable, which makes the framework applicable to a wider variety of tasks, as illustrated in the following subsections.

Table 2. Quantitative statistics of models reconstructed from meshes.

| Method   | CD $\times 10^{-3} \downarrow$ | HD $\times 10^{-2} \downarrow$ | NE $^\circ \downarrow$ | FC % $\uparrow$ |
|----------|--------------------------------|--------------------------------|------------------------|-----------------|
| NH-Rep   | 4.273                          | 3.081                          | 2.327                  | 96.59           |
| SharpNet | <b>3.788</b>                   | <b>2.249</b>                   | <b>2.286</b>           | <b>98.43</b>    |

**Boolean operations** Implicit CAD representations are naturally compatible with boolean operations, which are challenging to process using explicit representations such as splines and meshes. In Figure 12, we illustrate the application of SharpNet to constructive solid modeling.

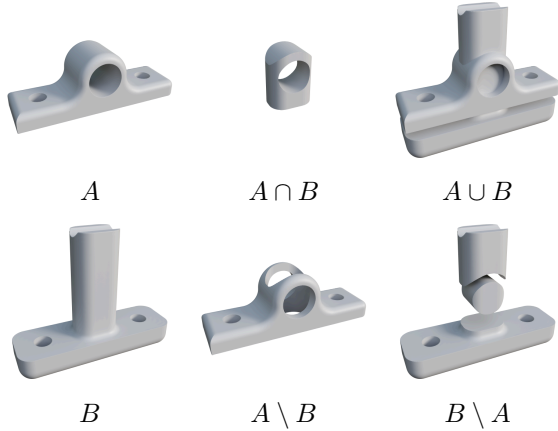


Figure 12. Boolean operations in SharpNet. Consider two CAD models,  $A$  and  $B$ , represented in SharpNet by their signed distance fields  $F_A$  and  $F_B$ , respectively. Because points inside  $A$  and  $B$  correspond to negative values of  $F_A$  and  $F_B$ , the Boolean operations intersection, union, and set difference can be expressed as  $F_{A \cap B} = \max(F_A, F_B)$ ,  $F_{A \cup B} = \min(F_A, F_B)$ ,  $F_{A \setminus B} = \max(F_A, -F_B)$ , and  $F_{B \setminus A} = \max(-F_A, F_B)$ .

## 5.2. CAD Models Learning from Point Clouds with Normals

We additionally assess our approach using only points together with their corresponding oriented normals as input, and compare it against InstantNGP (Müller et al., 2022). In contrast, NH-Rep (Guo et al., 2022) depends on pre-segmented patches and oriented normals and is therefore omitted from this comparison.

We train SharpNet using Equation (10), where MLP parameters  $\theta$  and feature surface points  $M$  are parameters to be learned. The loss components  $\mathcal{L}_{\text{sur}}$ ,  $\mathcal{L}_{\text{ext}}$ , and  $\mathcal{L}_{\text{ekl}}$  are identical to those defined in Equation (9). The regularization term  $\mathcal{L}_{\mathcal{R}}(M)$  is the same as in Equation (8), but it is now imposed on the boundary curves  $\partial M$ , rather than on  $M$  itself as in the 3D case, where  $M$  denotes surfaces.  $\mathcal{L}_{\mathcal{R}}$  is used to prevent  $M$  from self-intersection and folding.

$$\mathcal{L}(\theta, M) = \alpha_{\text{sur}} \cdot \mathcal{L}_{\text{sur}} + \alpha_{\text{ext}} \cdot \mathcal{L}_{\text{ext}} + \alpha_{\text{ekl}} \cdot \mathcal{L}_{\text{ekl}} + \alpha_{\text{nor}} \cdot \mathcal{L}_{\text{nor}} + \alpha_{\mathcal{R}} \cdot \mathcal{L}_{\mathcal{R}}. \quad (10)$$

The parameters are set to  $\alpha_{\text{sur}} = 7000$ ,  $\alpha_{\text{ext}} = 600$ ,  $\alpha_{\text{ekl}} = 35$ ,  $\alpha_{\text{nor}} = 15$ ,  $\alpha_{\mathcal{R}} = 10$  in our experiments.

The sharp features  $M$  in Equation (10) are learnable parameters that need to be initialized prior to training. The procedure for initializing  $M$  from a point cloud is described in detail in Appendix B.

As illustrated in Figure 13, when points and oriented normals instead of ground truth distances are used as constraints, the surfaces generated by InstantNGP (Müller et al., 2022) clearly exhibit bumpiness, because InstantNGP

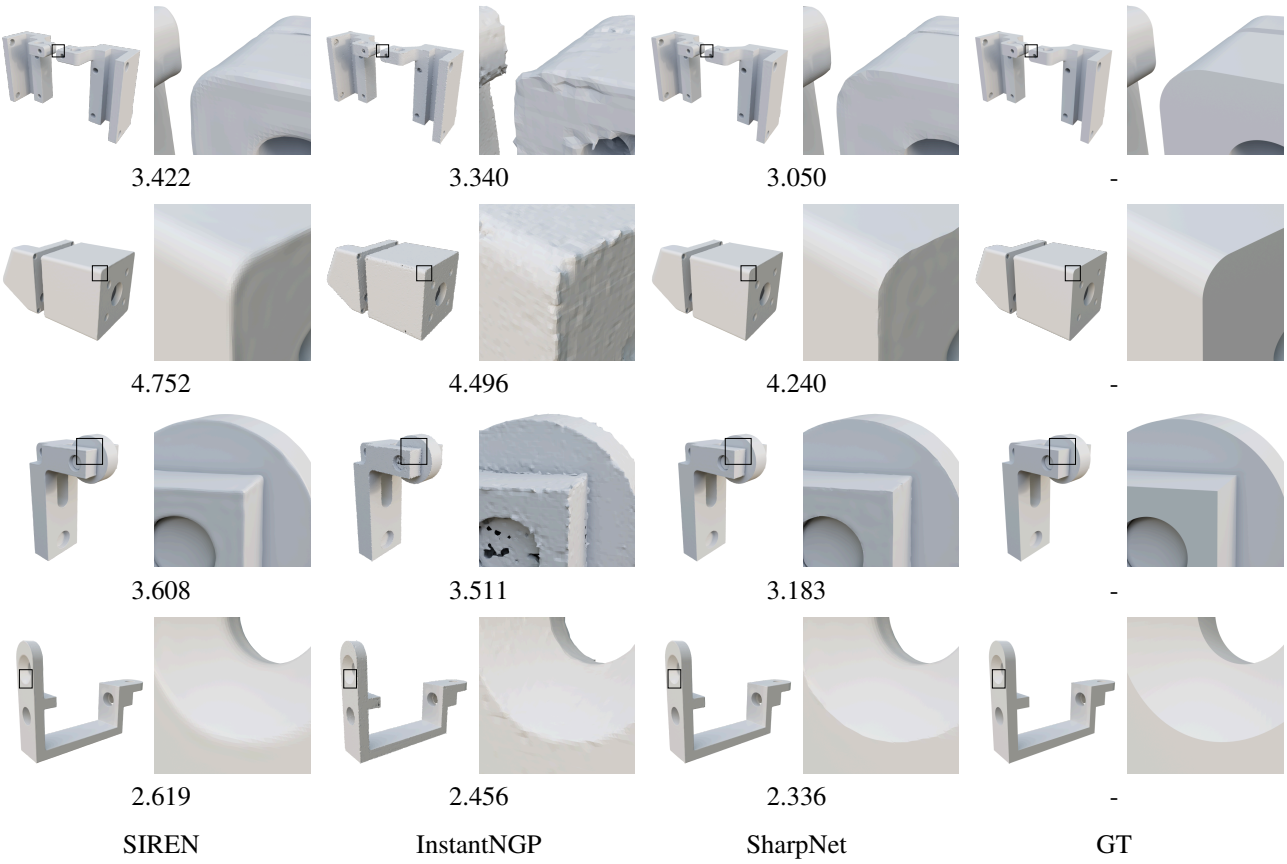


Figure 13. CAD models reconstructed from points and their associated oriented normals. The CD for each complete model is shown below each model.

adopts multiresolution hash grid encoding with linear interpolation resulting in only  $C^0$ -continuity at grid boundaries. Figure 14 visualizes CD errors using a color map, revealing that the instant NGP errors are especially large near sharp edges.

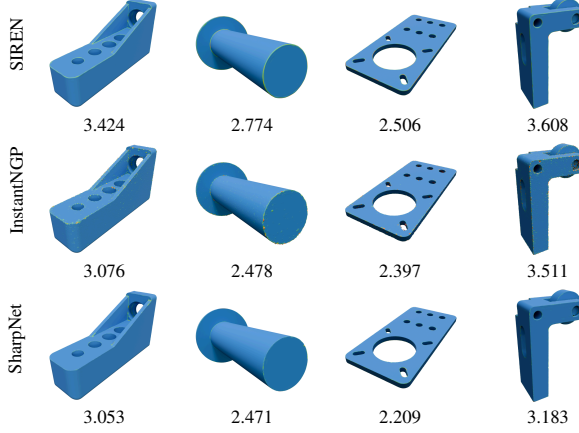


Figure 14. Illustration of CD errors by color map. The CD is shown below each model. Instant NGP produces many noisy points, particularly in regions around sharp edges.

As illustrated in Figure 15, when oriented normal supervision is removed, the performance of InstantNGP degrades significantly, resulting in a mixture of UDF and SDF, because its grid features are spatially localized and lack awareness of the overall geometry. A detailed analysis of SharpNet trained without normal supervision is provided in Section 5.3. Owing to its MLP-based architecture, SharpNet is well-suited for learning SDFs from point-only input.

The statistical metrics for the 100 testing models are summarized in Table 3. SharpNet clearly surpasses both SIREN and InstantNGP in performance.

Table 3. Quantitative statistics of models reconstructed from point clouds with oriented normals.

| Method     | CD $\times 10^{-3}$ $\downarrow$ | HD $\times 10^{-2}$ $\downarrow$ | NE $^\circ$ $\downarrow$ | FC % $\uparrow$ |
|------------|----------------------------------|----------------------------------|--------------------------|-----------------|
| SIREN      | 4.532                            | 4.119                            | 4.524                    | 96.28           |
| InstantNGP | 4.214                            | 3.325                            | 8.557                    | 95.88           |
| SharpNet   | <b>3.807</b>                     | <b>2.234</b>                     | <b>2.918</b>             | <b>98.09</b>    |

### 5.3. CAD Models Learning from Point Clouds

To further evaluate our method, we perform CAD reconstruction using only point clouds as input. NeurCADRecon (Dong et al., 2024) generates CAD models from point clouds by enforcing zero Gaussian curvature based solely on point cloud information. We compare our approach with the NeurCADRecon and SIREN baselines under the setting of point-cloud-only input.

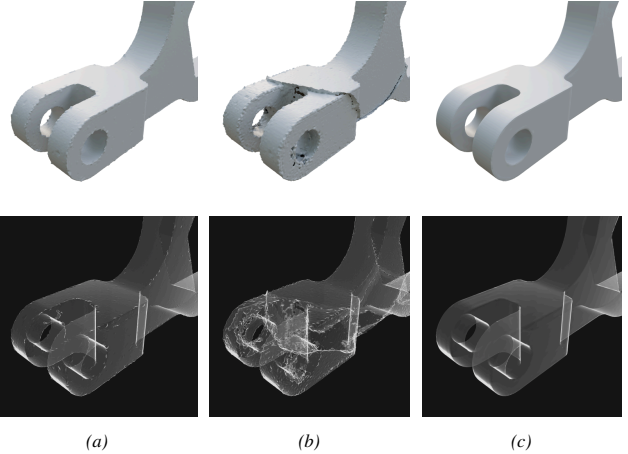


Figure 15. (a) InstantNGP (Müller et al., 2022) achieves good results under ground-truth SDF supervision, but in point-cloud reconstruction tasks, even with normal supervision, its lack of direct local feature correlation often leads to small artifacts away from the sampled points. (b) Without oriented-normal supervision, InstantNGP has a high probability of producing local normal flips, causing surface breakage at the boundary of normal flipped region, or degenerating into learning a UDF, resulting in missing or double-layered surfaces. (c) In contrast, SharpNet, equipped with learnable features, performs robustly even without normal supervision.

We optimize SharpNet using the loss in Equation (11), which is analogous to the loss in Equation (10), except that the normal component  $\mathcal{L}_{\text{nor}}$  is omitted.

$$\mathcal{L}(\theta, M) = \alpha_{\text{sur}} \cdot \mathcal{L}_{\text{sur}} + \alpha_{\text{ext}} \cdot \mathcal{L}_{\text{ext}} + \alpha_{\text{ekl}} \cdot \mathcal{L}_{\text{ekl}} + \alpha_{\mathcal{R}} \cdot \mathcal{L}_{\mathcal{R}}. \quad (11)$$

The parameters are set to  $\alpha_{\text{sur}} = 7000$ ,  $\alpha_{\text{ext}} = 600$ ,  $\alpha_{\text{ekl}} = 50$ , and  $\alpha_{\mathcal{R}} = 10$  in the experiment. The initialization of  $M$  is the same as that in Section 5.2.

Figure 16 presents the comparison results. While zero Gaussian curvature is advantageous for recovering sharp features, NeurCADRecon (Dong et al., 2024) still fails to reproduce clear, well-defined sharp structures because of the intrinsic smoothness of its MLP-based representation. The distributions of CD errors are shown in Figure 17. The quantitative statistics of the 100 testing models are listed in Table 4. Due to its controllable  $C^0$ -continuous representation, SharpNet surpasses NeurCADRecon in both visual quality and quantitative metrics. In fact, SharpNet has the potential to be a superior backbone for NeurCADRecon.

Table 4. Quantitative statistics of models reconstructed solely from points.

| Method       | CD $\times 10^{-3}$ $\downarrow$ | HD $\times 10^{-2}$ $\downarrow$ | NE $^\circ$ $\downarrow$ | FC % $\uparrow$ |
|--------------|----------------------------------|----------------------------------|--------------------------|-----------------|
| SIREN        | 4.593                            | 4.798                            | 5.877                    | 95.84           |
| NeurCADRecon | 4.354                            | 5.515                            | 5.388                    | 96.03           |
| SharpNet     | <b>4.129</b>                     | <b>4.004</b>                     | <b>3.839</b>             | <b>97.21</b>    |



Figure 16. CAD models reconstructed from points. The CD for each complete model is shown below each model.

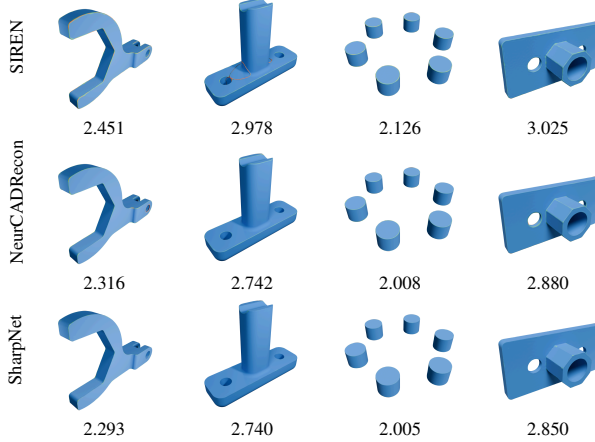


Figure 17. Illustration of CD errors by color map. The CD is shown below each model. NeurCADRecon exhibits noticeably large errors along sharp edges, because its plain MLP architecture is unable to accurately model perfectly sharp edges.

#### 5.4. Ablation Study

**Learning of feature set  $M$**  To evaluate the impact of feature set learning, we reconstruct CAD models from input points and oriented normals using the fixed initialized feature surface. During optimization of the loss function in Equation (11), the location of the points of  $M$  is kept fixed. The comparison in Figure 18 illustrates that, without a learnable  $M$ , noticeable artifacts appear along sharp edges, while allowing the learning of  $M$  largely eliminates these artifacts. To quantitatively assess the impact of learning, let  $S$  be the zero-level set of SharpNet. We obtain the zero-level curve  $L$  of SharpNet restricted to the feature set  $M$ , given by  $L = S \cap M$ , which represents the collection of non-smooth points on the reconstructed surface. We then compute the Chamfer distance between  $L$  and the ground-truth sharp edges, which we denote as the feature Chamfer distance (FCD). In addition, we evaluate the normals of  $M$  at sample points on  $L$  and compare them against the ground-truth normals; we refer to this quantity as the feature normal error (FNE) in degrees. Figure 19 shows the FCD and FNE distributions in the entire data set obtained with and without feature learning. It is clear that feature learning leads to substantial reductions in FCD and FNE compared to the use of fixed features.

**Mollifier** The performance of SharpNet depends mainly on the complexity of the feature set  $M$ . Let  $m$  denote the number of triangles in  $M$ . When training on  $n$  sampled points, the computational and memory complexity of SharpNet is  $O(mn)$ , which becomes a bottleneck when  $M$  is relatively complex. The mollifier transforms the global integral in Equation (5) into the local integral in Equation (6), reducing the complexity to approximately  $O(n)$  and thereby significantly lowering both the computation time and the

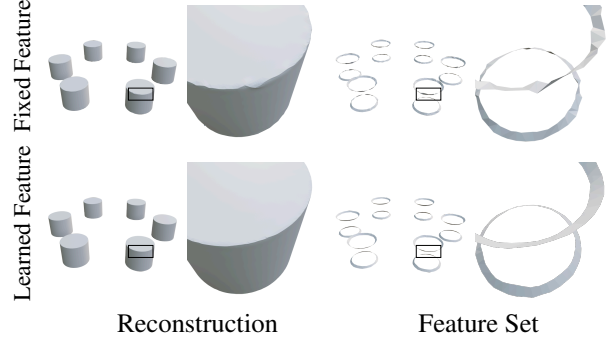


Figure 18. Feature set initialization obtained from point clouds is often inaccurate, and using it without optimization leads to noticeable artifacts around sharp edges in the CAD models. In contrast, optimizing the feature set significantly improves reconstruction quality around sharp features.

memory usage. We train SharpNet on a single NVIDIA RTX 4090 (24 GB) GPU and measure both training speed and memory consumption with and without the mollifier.

With the mollifier, SharpNet trains in about 20–34 minutes (23 minutes on average) and consumes 1.2–3.2 GB of GPU memory (1.9 GB on average). Without the mollifier, the Eikonal loss  $\mathcal{L}_{\text{ekl}}$  triggers out-of-memory errors during backpropagation due to its reliance on second-order derivatives. Even when reducing the number of sampled points per epoch to one tenth of the original, around 40% of experiments still encounter memory overflow. In this setting, the median training time rises to 110 minutes and the median memory usage reaches 15 GB. Considering that the non-mollified version uses only one tenth of the original samples, the mollifier yields nearly two orders of magnitude improvement in both training speed and memory efficiency.

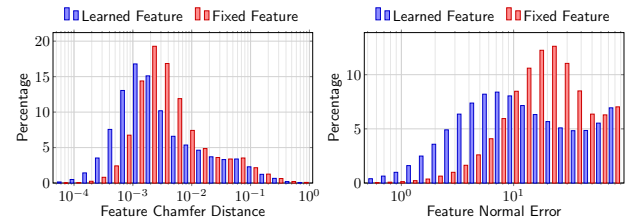


Figure 19. Histograms of the FCD and FNE distributions on a logarithmic scale. Both distance and angular errors exhibit a prominently shift toward zero after optimizing  $M$ . This suggests that optimizing  $M$  allows SharpNet to localize  $C^0$  features more accurately.

**Splitting of feature set  $M$**  The splitting of  $M$  enables the representation of a jump in the derivative difference. The jump may appear at sharp corners where concave and convex sharp curves meet. As illustrated in Figure 20, visible artifacts arise at these corners if no splitting is applied. Once splitting is performed, the corners are accurately re-

constructed, demonstrating that SharpNet can capture not only a normal derivative jump but also the discontinuity of the normal derivative jump.

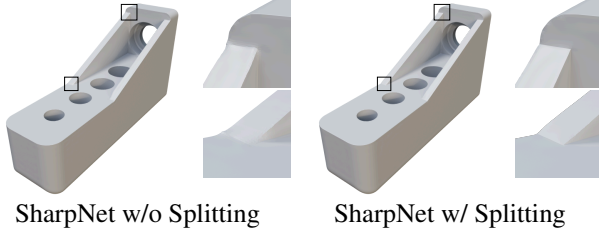


Figure 20. Without applying sharp curve splitting at joints, the corners of models produce artifacts, because of the discontinuity of gradient differences at these corners.

## 5.5. Limitations

In principle, the feature surface  $M$  may be any curve or surface. However, we discretize it into polylines or a triangular mesh to compute the integral efficiently, taking advantage of the fact that the Green's function integral admits closed-form expressions on polylines and triangular meshes.

The feature surface  $M$  must either be known beforehand or provided through an approximate initialization; it cannot be learned for the first time directly from scratch. Moreover, topological defects in  $M$ , such as cracks, cannot be corrected during the learning process.

## 6. Conclusions & Future Directions

We introduce SharpNet, a fully controllable  $C^0$ -continuous MLP-based representation. SharpNet maintains  $C^0$  continuity on the designated feature surface while remaining smooth elsewhere. Our meshless representation is more flexible and more precise than other representations, such as mesh-based approaches, which often introduce unnecessary  $C^0$  artifacts in regions that should be smooth. Moreover, our feature function has a differentiable closed-form expression, enabling the feature surface itself to be learned jointly with the MLP parameters. We assess SharpNet on various 2D tasks and CAD reconstruction problems. Our method can learn implicit neural CAD representations that preserve sharp edges, both when sharp edges are provided and when no sharp edge priors are available. Comparisons with several state-of-the-art baselines show that SharpNet achieves superior performance.

SharpNet can be extended to model non-differentiable features in time-varying signals or spatiotemporal fields, such as sharp transitions in motion or deformation data. Another promising direction is to represent higher-order discontinuities, such as jumps in curvature or other non-smooth differential quantities, by incorporating higher-order partial

differential equations in place of Poisson's equation. In addition, SharpNet can be generalized to represent  $C^{-1}$ -continuous functions, that is, functions that are discontinuous at user-specified locations. This extension would significantly broaden its applicability, especially for tasks involving abrupt transitions, including image vectorization, medical image segmentation, and scientific simulations with shocks or material interfaces. The generalization can be realized by relaxing the continuity condition in Equation (3) and applying Dirichlet boundary conditions that assign distinct function values on both sides of the feature set  $M$ . We identify this direction as an important avenue for future work.

## References

Belhe, Y., Gharbi, M., Fisher, M., Georgiev, I., Ramamoorthi, R., and Li, T.-M. Discontinuity-aware 2D neural fields. *ACM Transactions on Graphics*, 42(6), December 2023. ISSN 0730-0301. doi: 10.1145/3618379.

Chen, J., Shen, Z., Zhao, M., Jia, X., Yan, D.-M., and Wang, W. FR-CSG: Fast and reliable modeling for constructive solid geometry. *IEEE Transactions on Visualization and Computer Graphics*, 31(9):5869–5883, 2025. doi: 10.1109/TVCG.2024.3481278.

Costabel, M. Principles of boundary element methods. *Computer Physics Reports*, 6(1):243–274, 1987. ISSN 0167-7977. doi: 10.1016/0167-7977(87)90014-1.

Cybenko, G. Approximation by superpositions of a sigmoidal function. *Mathematics of Control, Signals and Systems*, 2(4):303–314, 1989. ISSN 1435-568X. doi: 10.1007/BF02551274.

Dong, Q., Xu, R., Wang, P., Chen, S., Xin, S., Jia, X., Wang, W., and Tu, C. NeurCADRecon: Neural representation for reconstructing cad surfaces by enforcing zero gaussian curvature. *ACM Transactions on Graphics*, 43(4), July 2024. ISSN 0730-0301. doi: 10.1145/3658171.

Du, T., Inala, J. P., Pu, Y., Spielberg, A., Schulz, A., Rus, D., Solar-Lezama, A., and Matusik, W. InverseCSG: automatic conversion of 3D models to CSG trees. *ACM Transactions on Graphics*, 37(6), December 2018. ISSN 0730-0301. doi: 10.1145/3272127.3275006.

Dupont, E., Cherenkova, K., Mallis, D., Gusev, G., Kacem, A., and Aouada, D. TransCAD: A hierarchical transformer for CAD sequence inference from point clouds. In *Computer Vision – ECCV 2024*, pp. 19–36, Cham, 2025. Springer Nature Switzerland. doi: 10.1007/978-3-031-73030-6\_2.

Erler, P., Guerrero, P., Ohrhallinger, S., Mitra, N. J., and Wimmer, M. Points2surf learning implicit sur-

faces from point clouds. In *Computer Vision – ECCV 2020*, pp. 108–124, Cham, 2020. Springer International Publishing. ISBN 978-3-030-58558-7. doi: 10.1007/978-3-030-58558-7\_7.

Guo, H.-X., Liu, Y., Pan, H., and Guo, B. Implicit conversion of manifold B-rep solids by neural halfspace representation. *ACM Transactions on Graphics*, 41(6), November 2022. ISSN 0730-0301. doi: 10.1145/3550454.3555502.

Hornik, K. Approximation capabilities of multilayer feed-forward networks. *Neural Networks*, 4(2):251–257, 1991. ISSN 0893-6080. doi: 10.1016/0893-6080(91)90009-T.

Imaizumi, M. and Fukumizu, K. Deep neural networks learn non-smooth functions effectively. In *Proceedings of the Twenty-Second International Conference on Artificial Intelligence and Statistics*, volume 89 of *Proceedings of Machine Learning Research*, pp. 869–878. PMLR, April 2019.

Ismailov, V. E. A three layer neural network can represent any multivariate function. *Journal of Mathematical Analysis and Applications*, 523(1):127096, 2023. ISSN 0022-247X. doi: 10.1016/j.jmaa.2023.127096.

Ju, T., Losasso, F., Schaefer, S., and Warren, J. Dual contouring of hermite data. *ACM Transactions on Graphics*, 21(3):339–346, July 2002. ISSN 0730-0301. doi: 10.1145/566654.566586.

Kingma, D. P. and Ba, J. Adam: A method for stochastic optimization. In *3rd International Conference on Learning Representations, ICLR 2015, San Diego, CA, USA, May 7-9, 2015, Conference Track Proceedings*, 2015.

Koch, S., Matveev, A., Jiang, Z., Williams, F., Artemov, A., Burnaev, E., Alexa, M., Zorin, D., and Panizzo, D. Abc: A big cad model dataset for geometric deep learning. In *2019 IEEE/CVF Conference on Computer Vision and Pattern Recognition (CVPR)*, pp. 9593–9603, 2019. doi: 10.1109/CVPR.2019.00983.

Li, Q., Feng, H., Shi, K., Fang, Y., Liu, Y.-S., and Han, Z. Neural gradient learning and optimization for oriented point normal estimation. In *SIGGRAPH Asia 2023 Conference Papers*, SA '23, New York, NY, USA, 2023. Association for Computing Machinery. ISBN 9798400703157. doi: 10.1145/3610548.3618253.

Li, Y., Wang, H., Liu, Y., Huang, J., Liu, S., Huang, C., Guo, J., Guo, J., and Guo, Y. Deep point cloud edge reconstruction via surface patch segmentation. *IEEE Transactions on Visualization and Computer Graphics*, 31(10):7463–7477, 2025. doi: 10.1109/TVCG.2025.3547411.

Lin, G., Yang, L., Zhang, C., Pan, H., Ping, Y., Wei, G., Komura, T., Keyser, J., and Wang, W. Patch-Grid: An efficient and feature-preserving neural implicit surface representation. *ACM Transactions on Graphics*, 44(2), April 2025. ISSN 0730-0301. doi: 10.1145/3727142.

Liu, C., Wang, S., Fisher, M., Aneja, D., and Jacobson, A. 2D neural fields with learned discontinuities. *Computer Graphics Forum*, pp. e70023, 2025a. doi: 10.1111/cgf.70023.

Liu, M., Chang, Y., Wang, Z., Chen, P. Y., and Grinspun, E. Precise gradient discontinuities in neural fields for subspace physics. In *Proceedings of the SIGGRAPH Asia 2025 Conference Papers*, SA Conference Papers '25, New York, NY, USA, 2025b. Association for Computing Machinery. ISBN 9798400721373. doi: 10.1145/3757377.3763810.

Liu, Y., Chen, J., Pan, S., Cohen-Or, D., Zhang, H., and Huang, H. Split-and-fit: Learning b-reps via structure-aware voronoi partitioning. *ACM Trans. Graph.*, 43(4), July 2024a. ISSN 0730-0301. doi: 10.1145/3658155.

Liu, Y., Obukhov, A., Wegner, J. D., and Schindler, K. Point2CAD: Reverse engineering CAD models from 3D point clouds. In *2024 IEEE/CVF Conference on Computer Vision and Pattern Recognition (CVPR)*, pp. 3763–3772, 2024b. doi: 10.1109/CVPR52733.2024.00361.

Liu, Z., Wang, Y., Vaidya, S., Ruehle, F., Halverson, J., Soljacic, M., Hou, T. Y., and Tegmark, M. KAN: Kolmogorov–arnold networks. In *The Thirteenth International Conference on Learning Representations*, 2025c.

Ma, B., Han, Z., Liu, Y.-S., and Zwicker, M. Neural-pull: Learning signed distance function from point clouds by learning to pull space onto surface. In *Proceedings of the 38th International Conference on Machine Learning*, volume 139 of *Proceedings of Machine Learning Research*, pp. 7246–7257. PMLR, July 2021.

Mescheder, L., Oechsle, M., Niemeyer, M., Nowozin, S., and Geiger, A. Occupancy networks: Learning 3D reconstruction in function space. In *2019 IEEE/CVF Conference on Computer Vision and Pattern Recognition (CVPR)*, pp. 4455–4465, Los Alamitos, CA, USA, June 2019. doi: 10.1109/CVPR.2019.00459.

Mildenhall, B., Srinivasan, P. P., Tancik, M., Barron, J. T., Ramamoorthi, R., and Ng, R. NeRF: Representing scenes as neural radiance fields for view synthesis. In *Computer Vision – ECCV 2020*, pp. 405–421, Cham, 2020. Springer International Publishing. ISBN 978-3-030-58452-8. doi: 10.1007/978-3-030-58452-8\_24.

Müller, T., Evans, A., Schied, C., and Keller, A. Instant neural graphics primitives with a multiresolution hash encoding. *ACM Transactions on Graphics*, 41(4), July 2022. ISSN 0730-0301. doi: 10.1145/3528223.3530127.

Pang, B., Zheng, Z., Wang, G., and Wang, P.-S. Learning the geodesic embedding with graph neural networks. *ACM Transactions on Graphics*, 42(6), December 2023. ISSN 0730-0301. doi: 10.1145/3618317.

Park, J. J., Florence, P., Straub, J., Newcombe, R., and Lovegrove, S. DeepSDF: Learning continuous signed distance functions for shape representation. In *2019 IEEE/CVF Conference on Computer Vision and Pattern Recognition (CVPR)*, pp. 165–174, 2019. doi: 10.1109/CVPR.2019.00025.

Sharma, G., Goyal, R., Liu, D., Kalogerakis, E., and Maji, S. Neural shape parsers for constructive solid geometry. *IEEE Transactions on Pattern Analysis and Machine Intelligence*, 44(5):2628–2640, 2022. doi: 10.1109/TPAMI.2020.3044749.

Shen, Z., Zhao, M., Yan, D.-M., and Wang, W. Mesh2Brep: B-rep reconstruction via robust primitive fitting and intersection-aware constraints. *IEEE Transactions on Visualization and Computer Graphics*, 31(10):6661–6676, 2025. doi: 10.1109/TVCG.2025.3525844.

Sitzmann, V., Martel, J. N., Bergman, A. W., Lindell, D. B., and Wetzstein, G. Implicit neural representations with periodic activation functions. In *Advances in Neural Information Processing Systems*, volume 33, pp. 7462–7473. Curran Associates, Inc., 2020.

Sorkine, O. Differential representations for mesh processing. *Computer Graphics Forum*, 25(4):789–807, 2006. doi: 10.1111/j.1467-8659.2006.00999.x.

Takikawa, T., Litalien, J., Yin, K., Kreis, K., Loop, C., Nowrouzezahrai, D., Jacobson, A., McGuire, M., and Fidler, S. Neural geometric level of detail: Real-time rendering with implicit 3d shapes. In *2021 IEEE/CVF Conference on Computer Vision and Pattern Recognition (CVPR)*, pp. 11353–11362, 2021. doi: 10.1109/CVPR46437.2021.01120.

Usama, M., Khan, M. S., Stricker, D., and Afzal, M. Z. NURBGen: High-fidelity text-to-CAD generation through LLM-driven NURBS modeling. In *Proceedings of the AAAI Conference on Artificial Intelligence*, 2026.

Wang, P., Liu, L., Liu, Y., Theobalt, C., Komura, T., and Wang, W. Neus: Learning neural implicit surfaces by volume rendering for multi-view reconstruction. In *Advances in Neural Information Processing Systems*, volume 34, pp. 27171–27183. Curran Associates, Inc., 2021.

Wang, P., Dong, Q., Liang, F., Pan, H., Yang, L., Zhang, C., Lin, G., Zhang, C., Zhou, Y., Tu, C., Xin, S., Sheffer, A., Li, X., and Wang, W. Neuvas: Neural implicit surfaces for variational shape modeling. *ACM Trans. Graph.*, 44(6), December 2025. ISSN 0730-0301. doi: 10.1145/3763331.

Wang, Y., Rahmann, L., and Sorkine-Hornung, O. Geometry-consistent neural shape representation with implicit displacement fields. In *The Tenth International Conference on Learning Representations, ICLR 2022, Virtual Event, April 25-29, 2022*. OpenReview.net, 2022.

Wu, Q., Xu, K., and Wang, J. Constructing 3D CSG models from 3D raw point clouds. *Computer Graphics Forum*, 37(5):221–232, 2018. doi: 10.1111/cgf.13504.

Yu, F., Chen, Z., Li, M., Sanghi, A., Shayani, H., Mahdavi-Amiri, A., and Zhang, H. Capri-net: Learning compact cad shapes with adaptive primitive assembly. In *2022 IEEE/CVF Conference on Computer Vision and Pattern Recognition (CVPR)*, pp. 11758–11768, 2022. doi: 10.1109/CVPR52688.2022.01147.

Yu, F., Chen, Q., Tanveer, M., Mahdavi Amiri, A., and Zhang, H. D<sup>2</sup>CSG: Unsupervised learning of compact CSG trees with dual complements and dropouts. In *Advances in Neural Information Processing Systems*, volume 36, pp. 22807–22819. Curran Associates, Inc., 2023.

Zhu, X., Du, D., Chen, W., Zhao, Z., Nie, Y., and Han, X. NerVE: Neural volumetric edges for parametric curve extraction from point cloud. In *2023 IEEE/CVF Conference on Computer Vision and Pattern Recognition (CVPR)*, pp. 13601–13610, 2023. doi: 10.1109/CVPR52729.2023.01307.

## A. Feature Surface Construction from Mesh

Given a CAD triangular mesh as input, sharp edges are identified by evaluating the dihedral angle between each pair of triangles that share an edge. As illustrated in Figure 21(a), we obtain the sharp curve set, where the dihedral angles are smaller than a user specified threshold. The sharp curve set is represented as an undirected graph  $\mathcal{S}$  composed of all sharp edges together with their incident vertices. Next, we construct the feature surface  $M$  by expanding  $\mathcal{S}$  along certain guiding directions to form a strip-like surface  $M$  that approximates the medial surface near the sharp edges. As illustrated in Figure 21(b), for each sharp edge  $e_i \in \mathcal{S}$ , we compute the angular bisector plane of its two adjacent triangle faces, which serves as an approximation of the local medial surface. For every edge  $e_i \in \mathcal{S}$ , we then compute a guiding direction  $g_{e_i}$  of a unit vector, defined as a vector orthogonal to  $e_i$  and lying within its bisector plane, pointing to the model exterior.

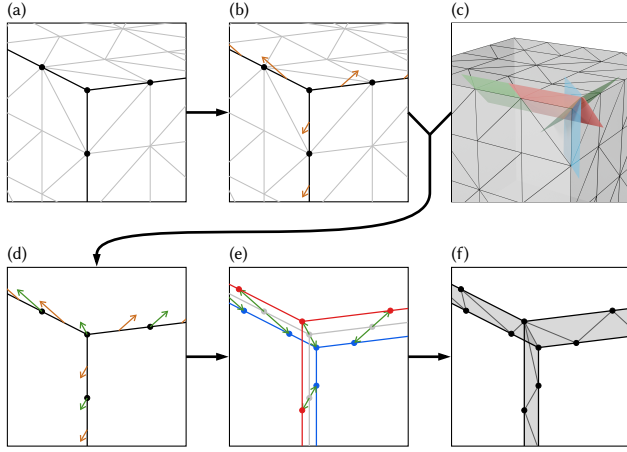


Figure 21. For 3D tasks, the  $C^0$  feature surface  $M$  of SharpNet can be constructed either from a mesh or directly from a point cloud. (a) Sharp edges identified from the input mesh. (b) Guiding directions computed for each sharp edge. (c) Local bisector planes associated with the sharp edges. (d) Guiding directions propagated from edges to all vertices, chosen to lie as closely as possible within the local bisector planes of the incident edges. (e) Each feature vertex is offset bidirectionally along its guiding direction to generate the feature surface  $\partial M$ . (f) The strip-like triangular mesh  $M$ .

As illustrated in Figure 21(c)(d), these edge-based guiding directions are subsequently propagated to all vertices  $v_j$  of  $\mathcal{S}$  to obtain vertex guiding directions  $g_{v_j}$ . For a vertex  $v$ , let  $\mathbf{E}_v$  denote the set of all edges incident to  $v$ . When  $\|\mathbf{E}_v\| = 1$ , i.e., when the degree satisfies  $\deg(v) = 1$ , the vertex  $v$  is an end vertex, and we directly assign its guiding direction  $g_v$  to be identical to the guiding direction  $g_e$  of its unique incident edge  $e$ . When  $\|\mathbf{E}_v\| > 1$ , we require  $g_v$  to align as closely as possible with the bisector planes of all edges in  $\mathbf{E}_v$ , meaning that the dot product between  $g_v$  and the normal of each bisector plane should be as close to zero as

possible. Although the mean of the edge guiding directions  $\sum_{e \in \mathbf{E}_v} g_e / \|\mathbf{E}_v\|$  provides a reasonable approximation, it is not exact. Ideally, as shown in Figure 21(c), the bisector planes of all incident edges should intersect along a single line, and we take the direction of this line as  $g_v$ .

Taking all the above considerations into account, we determine the guiding direction  $g_v$  for any vertex  $v$  by minimizing the following energy:

$$E_v = \{e_i \mid e_i \in \mathbb{S}, e_i \ni v\}$$

$$g_v = \arg \min_{g \in \mathbb{S}^2} \sum_{e_i \in \mathbf{E}_v} |g \cdot (g_{e_i} \times \frac{\vec{e}_i}{\|\vec{e}_i\|})| + \lambda \cdot \|g - \frac{\sum_{e_i \in \mathbf{E}_v} g_{e_i}}{\|\mathbf{E}_v\|}\|,$$

where  $\mathbb{S}^2$  denotes the unit sphere. The first term of the energy encourages  $g_v$  to align with the bisector planes of the incident edges, while the second term prevents  $g_v$  from deviating too far from the mean of the edge directions  $\{g_{e_i}\}$ , providing additional robustness in the optimization and correctly handling vertices of degree one, where the vertex lies at the end of a sharp edge.

Given a prescribed width parameter  $w$ , we offset each vertex  $v \in \mathcal{S}$  along its guiding direction  $g_v$  by  $\pm w$ . This bidirectional displacement transforms the polyline feature set  $\mathcal{S}$  into a strip-like surface  $M$ , as illustrated in Figure 21(e)(f). By construction,  $M$  lies in close proximity to the original mesh surface and serves as a localized representation of the surface where the distance field exhibits a directional derivative jump.

## B. Feature Surface Initialization from Points

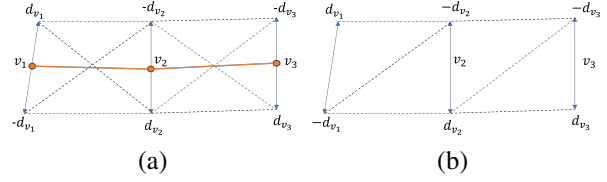


Figure 22. Feature surface generation. (a) For each  $d_{v_i}$ , we create offsets in both directions,  $d_{v_i}$  and  $-d_{v_i}$ . We then examine the two possible connection configurations:  $\{(d_{v_i}, d_{v_j}), (-d_{v_i}, -d_{v_j})\}$  (black dashed lines) and  $\{(-d_{v_i}, d_{v_j}), (d_{v_i}, -d_{v_j})\}$  (green dashed lines). (b) We choose the configuration whose paired connections are more parallel to construct the feature surface. The extra diagonal lines divide the rectangle into triangles.

Given a point cloud as input, since the dihedral angles cannot be computed directly, we adopt NerVE (Zhu et al., 2023) to initialize the sharp curve set  $\mathcal{S}$  from the point cloud itself. Similarly, the angular bisector plane required for extracting the feature surface  $M$  cannot be evaluated from the point cloud. Instead, we estimate a coarse guiding direction  $d_v$  for each vertex  $v \in \mathcal{S}$  by forming a vector from the centroid of  $v$ 's 32 nearest neighbors in the point cloud to  $v$ . Finally, we

offset all  $v \in S$  in both directions of  $d_v$  and  $-d_v$  to generate the stripe-like feature surface  $M$ . As shown in Figure 22, because  $d_v$  cannot be given a consistent orientation, some  $d_{v_i}$  may point in the opposite direction. To prevent rectangles from folding, we evaluate both connection patterns (the black and green dashed segment pairs) and select the one that is closer to being parallel.